1990-09

Modeling Studies of Eddies in the Leeuwin Current: The Role of Thermal Forcing

Batteen, Mary L.

Journal of Physical Oceanography, Vol. 20, pp. 1484-1520.
http://hdl.handle.net/10945/47167

Modeling Studies of Eddies in the Leeuwin Current: The Role of Thermal Forcing

MARY L. BATTEEN AND MARTIN J. RUTHERFORD*

Department of Oceanography, Naval Postgraduate School, Monterey, California

(Manuscript received 29 November 1989, in final form 5 April 1990)

ABSTRACT

A high resolution, multilevel, primitive equation (PE) model is used to investigate the generation and stability of the Leeuwin Current and eddies off the west coast of Australia. Two numerical experiments are conducted to investigate the roles of the Indian Ocean temperature field and the North West (NW) Shelf waters in generating both the current and eddies. In the first experiment an alongshore temperature gradient, typical of the Indian Ocean temperature field, is imposed, while in the second experiment the additional effects of the NW Shelf waters are considered. In the first experiment, the meridional Indian Ocean temperature gradient is sufficient to drive a poleward surface flow (the Leeuwin Current) and an equatorial undercurrent. The surface flow is augmented by onshore geostrophic flow and accelerates downstream. In the second experiment, the inclusion of the NW Shelf waters completely dominates in the NW Shelf equatorial source region. The effects of the NW Shelf waters weaken away from the source region but they continue to augment the Indian Ocean forcing, resulting in a stronger flow along the entire coastal boundary. The currents generated by the model agree well with the Leeuwin Current Interdisciplinary Experiment (LUCIE) current meter observations obtained during the austral fall and winter, when the Leeuwin Current is observed, and other recent modeling studies.

The current is unstable and has significant mesoscale variability. The current forced only by the alongshore temperature gradient is unstable toward the poleward end of the model domain. In this region, barotropic instability tends to dominate over baroclinic instability. When the NW Shelf waters are added to force the current, eddies are generated near the source of these waters (in the equatorward end of the model domain) through barotropic instability of the current. Farther downstream, the NW Shelf waters add strong baroclinicity, which weakens poleward, to the current. Eddies are subsequently generated downstream from the NW Shelf region through both baroclinic and barotropic instability processes.

Several scales of eddies are found to be dominant. The forcing by the Indian Ocean leads to eddy growth on scales around 150 km. With the inclusion of the NW Shelf waters, the wavelength associated with mesoscale variability is around 180 km. Both of these length scales are close to the wavelength associated with a low-mode Rossby radius of deformation. The eddies generated by the model compare well with available observations.

This study shows that the Leeuwin Current can be successfully modeled using a PE model forced by the mean climatology. Consistent with the findings of recent modeling studies, a shelf is not required to produce and maintain the current. The mesoscale features which have been missing from previous modeling studies are produced by the model and at scales comparable with available observations.

1. Introduction

The Leeuwin Current is a surface flow of warm, low-salinity, tropical water, poleward along the west coast of Australia, then eastward into the Great Australian Bight. It appears to have its source in the northeast Indian Ocean and extends to Australia's southern coastal waters, having been reported as far east as 142°E (Godfrey et al. 1986) and 130°E (Rochford 1986).

The current is narrow (<100 km wide), shallow (generally <300 m), has an underlying equatorward flow and is strongly seasonal in nature (for excellent reviews of the current, see Church et al. 1989; Weaver and Middleton 1989). Off the west coast of Australia, the maximum flow occurs along the southern portion of the North West (NW) Shelf (22°S) from February to June (Holloway and Nye 1985). Based on observations from the Leeuwin Current Interdisciplinary Experiment (LUCIE) reported by Boland et al. (1988), the maximum flow occurs off Dongara (29.5°S) from April to June and further south at Cape Mentelle (34°S) from June to July (see Fig. 1 for geographical locations). The flow's eastward limit south of Australia is reached in July (Rochford 1986).

The Leeuwin Current differs markedly in its characteristics, and hence presumably in its associated dynamics, from currents found in other eastern ocean regions. The other major eastern boundary currents, i.e., Peru, California, Benguela, and Canary, are characterized by climatologically weak (<10 cm s^{-1}) surface flow toward the equator, cold upwelled water at

* Present affiliation: Australian Joint Maritime War Centre, Naval Air Station, New South Wales, Australia 2541.

Corresponding author address: Dr. Mary L. Batteen, Department of Oceanography, Naval Postgraduate School, Monterey, CA 93943-5000.

the surface, shallow (<30 m depth) thermoclines and high biological production (Parrish et al. 1983). In contrast, the Leeuwin Current has a poleward surface flow that exceeds 150 cm s^{-1} at times (Cresswell and Golding 1980; Godfrey et al. 1986), anomalously warm water, downwelling, a deep (>50 m) thermocline (Thompson 1984) and low fish production. The other currents are part of the subtropical anticyclonic gyres that are driven primarily by the anticyclonic wind fields, and variations in current strength are highly coherent with variations in local wind stress (Allen 1980; Huyer 1990). With such markedly different features, the Leeuwin Current may be expected to depart just as markedly in its generation mechanisms and dynamic features.

Within the past decade alone, there have been extensive modeling and observational studies of the Leeuwin Current. Because the results of these as well as previous investigations are pertinent to the present study, we present a brief historical survey of observational, modeling, and theoretical studies of the Leeuwin Current and its eddies. The survey will show that, despite extensive investigations, a complete explanation is missing for the Leeuwin Current, its different features (in comparison with other eastern boundary currents) and its eddies.

a. Observational studies of the Leeuwin Current

The earliest documentation of the characteristics of a poleward flowing current (named the Leeuwin Current by Cresswell and Golding 1980, in honor of the first Batavia-bound Dutch vessel to explore the southwest of Australia) was by Saville-Kent (1897) following studies of the marine fauna of the Abrolhos Islands (28.5°S). Anomalously warm water was found around the Islands but not on the mainland coast 50 miles to the east where temperatures were about 7°C cooler. This led to a suggestion that the water must be transported to the region. Dakin (1919) noted that the temperature difference between the Abrolhos Islands and the mainland was greatest in the austral winter. Rochford (1969) used drift bottles to ascertain that the poleward flow in the austral winter extended to the south of Rottnest Island (32°S) and that a flow reversal occurred in the austral summer. The reversal was also apparent in salinity records for the southwest coast of Australia. The salinity variation was over twice that attributable to evaporation and precipitation; hence, the salinity became an effective tracer of the flow regime in the region. Kitani (1977) observed low salinity water at 32°S in November 1975, which showed that the occurrence of tropical water was not confined to the austral winter. The eastward continuation of the poleward flow into the Great Australian Bight was inferred by Colborn (1975) from temperature data, and by Markina (1976) from plankton data, which further emphasized its strong signal.

The deployment of satellite-tracked drifting buoys off Western Australia from 1975 to 1977 added a new dimension to the data collected on the circulation features. Cresswell and Golding (1979) illustrated the spatial and temporal complexity of the current in charts of buoy tracks and showed clear evidence for the existence of mesoscale eddies on the western side of the current. The buoys were observed to accelerate as they entered the current and to slow again in their departure providing evidence of a high speed core current that was measured at up to 170 cm s^{-1} from buoy positions.

High spatial resolution ($\sim$1 km) and temperature discrimination (<0.1°C) of both infrared and Advanced Very High Resolution Radiometer (AVHRR) imagery since the mid-1970s have been used to reveal the temperature contrasts between the different currents and cyclonic and anticyclonic eddies off the coast of Western Australia. For example, the satellite image of Pearce and Cresswell (1985) shows a large wedge of warm water in the northeast Indian Ocean being funneled into a narrow current near North West Cape, then moving south along the shelf and slope until reaching Cape Leeuwin, where it abruptly swings eastward and extends across the Great Australian Bight. Mesoscale features can be seen off Perth, and filament-like features can be seen off the south coast.

Between September 1986 and August 1987, the most extensive current meter measurements of the Leeuwin Current to date were made as part of the LUCIE experiment, coordinated by the CSIRO Division of Oceanography. The data, reported by Boland et al. (1988), show that the current is weakest from September to February and strongest from February to August. The measurements also show the presence of an equatorward undercurrent and an acceleration of the Leeuwin Current poleward.

b. Modeling studies of the Leeuwin Current

Thompson and Veronis (1983) were the first to model the Leeuwin Current. They suggested that local winds on the NW Shelf could generate the current. This theory was refuted by the current meter observations of Holloway and Nye (1985). It was also rejected by Thompson (1984), who proposed instead an alongshore steric height gradient as the primary forcing mechanism with the winter deepening of the mixed layer offsetting the effects of the equatorward wind stress. Godfrey and Ridgway (1985) quantified the contributions of the alongshore pressure gradient and equatorward wind stress and strongly supported Thompson's (1984) finding. They further proposed that flow from the Pacific Ocean through the Indonesian Archipelago to the northeast Indian Ocean could be responsible for the large steric height gradient, a feature which makes the Leeuwin Current unique among eastern boundary currents.

McCreary et al. (1986) rejected the throughflow as

being a primary forcing mechanism and proposed that thermohaline gradients were responsible for the alongshore pressure gradient. Their model results showed a poleward surface current and equatorward undercurrent comparable in strength to observations, but no mesoscale features were shown. Kundu and McCreary (1986) examined the throughflow theory separately and produced a weak poleward flow. They concluded that the throughflow was a secondary forcing mechanism.

Thompson (1987) used an analytic model of the Leeuwin Current to investigate why the flow is poleward and why no upwelling occurs, despite the upwelling-favorable wind. He concluded that the wind-mixed (or surface Ekman) layer is deep enough to reduce the effects of wind forcing below the level of the forcing due to the poleward pressure gradient.

Gentilli (1972) suggested that a seasonal (austral autumn and winter) throughflow could be isolated in the northeast Indian Ocean during the austral summer, providing a source for the subsequent Leeuwin Current generation. This theory is supported by the satellite image of Pearce and Cresswell (1985) of a large wedge-shaped mass of warm water off northwest Australia funneling into a poleward current. Weaver and Middleton (1989) used a Bryan–Cox ocean general circulation model to investigate the contributions to the Leeuwin Current from both the alongshore density gradient and the warmer, fresher NW Shelf waters. The model, which includes simple coastal geography and topography, produced a realistic Leeuwin Current, but the current lacks mesoscale variability. Weaver and Middleton (1989) concluded that the Leeuwin Current is a baroclinic current driven by the alongshore density gradient. They also believe the current is strengthened locally, by barotropic enhancement, in the vicinity of the source of the NW Shelf waters.

c. *Theories for the Leeuwin Current*

Despite extensive modeling studies throughout the 1980s, a complete explanation for the Leeuwin Current and its different features, in comparison with other eastern boundary currents, remains outstanding. A synopsis of recent theories is presented here. There is general agreement (e.g., by Thompson 1987; Godfrey and Ridgway 1985; McCreary et al. 1986; Pearce and Cresswell 1985; Weaver and Middleton 1989) that the Leeuwin Current is generated by a meridional pressure gradient that overwhelms the opposing equatorward wind stress. The wind forcing effects are diminished by deep mixed layers (Thompson 1987), possibly

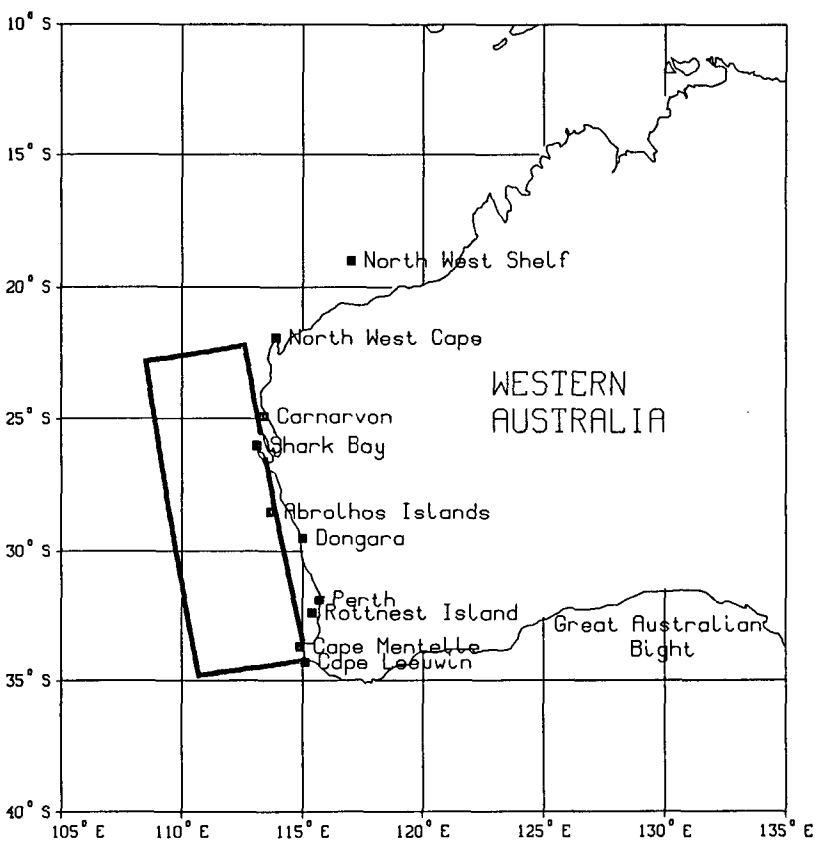

FIG. 1. Study domain. The rectangle represents the primitive equation (PE) model domain.

TABLE 1. Initial temperature (°C) for Indian Ocean.

Latitude (°S)	Layer									
	1	2	3	4	5	6	7	8	9	10
22	24.0	22.9	21.6	19.2	14.5	9.4	5.9	3.5	2.0	1.0
24	23.3	22.3	20.9	18.6	14.3	9.4	5.9	3.5	2.0	1.0
26	22.6	21.7	20.3	18.0	14.1	9.3	5.9	3.5	2.0	1.0
28	22.0	21.0	19.7	17.4	13.9	9.3	5.9	3.5	2.0	1.0
30	21.3	20.4	19.0	16.7	13.6	9.2	5.8	3.5	2.0	1.0
32	20.6	19.8	18.4	16.1	13.4	9.2	5.8	3.5	2.0	1.0
34	19.9	19.1	17.7	15.5	13.2	9.1	5.8	3.5	2.0	1.0

formed in response to a strong heat flux out of the ocean, which is a feature unique to the Leeuwin Current among eastern boundary currents (Hsiung 1985; Godfrey and Weaver 1990; Weaver and Middleton 1990). The source of the Leeuwin Current water is predominantly geostrophic inflow from the west (McCreary et al. 1986; Thompson 1987) and is augmented by a source from the NW Shelf (Kundu and McCreary 1986; Weaver and Middleton 1989), possibly having its origin in the Pacific Ocean (Godfrey and Ridgway 1985). The inflow of the NW Shelf waters is consistent with the warm, low-salinity signature of the Leeuwin Current surface waters. The results of Weaver and Middleton (1989) suggest that poleward gradients of both temperature and salinity are sufficient to establish a pressure gradient strong enough to support the observed flow. Godfrey and Weaver (1990) propose enhancement of this pressure gradient by the buildup of warm, fresh water near Indonesia due to the action of zonal winds in the equatorial Pacific. In particular, they argue that channels through the Indonesian Archipelago are crucial for the existence of the Leeuwin Current by allowing the continuity of warm, fresh waters from the western equatorial Pacific coast through to the northwest tip of Australia. Internal Kelvin waves propagate along the coast of Western Australia radiating internal Rossby waves westward, trying to maintain the specific volume anomaly profile off Western Australia equal to that at the northwest tip of Australia. Convective surface cooling then occurs poleward of about 20°S, and the deep Indian Ocean alongshore density gradient is set up.

d. Mesoscale variability

One of the major gaps in Leeuwin Current research is in the area of the complex eddy fields found in the current. While observational (e.g., Hamon and Cresswell 1972; Golding and Symonds 1978; Cresswell and Golding 1979, 1980; Andrews 1977, 1983; Griffiths and Pearce 1985) and laboratory (e.g., Condie and Ivey 1988) studies reveal the nature and characteristics of the mesoscale features, no modeling studies have successfully produced eddy fields which would allow analysis of their generation mechanisms.

The existence of eddies in the eastern Indian Ocean was first postulated by Wyrtki (1962). Using dynamic height calculations relative to 1750 decibars, he showed a strong semipermanent eddy present near 32°S, 110°E with cyclonic circulation above the reference level and anticyclonic below. Analysis by Hamon (1965) suggested a double eddy structure in the region 30°–32°S, east of 107°E during the austral winter period of late April to November. In a subsequent study, Hamon (1972) found little seasonal variation in dynamic height anomalies in the same area, although a tendency toward greater variability during the months from August to November was noted.

Andrews (1977) investigated mesoscale features in the region and observed nearly zonal planetary Rossby waves in the West Australian Current and nearly meridional coastal waves in the coastal current south of 15°S, where zonal inflow occurred. The interaction of the two wave types, particularly in the vicinity of a large trough, resulted in meandering in both currents. No clear ringlike features (i.e., closed isopleths of velocity and temperature at several depths) were apparent to Andrews in his study, although some mixed layer and surface temperature rings were analyzed. Andrews (1983) attempted to reconcile the apparently contradictory findings of Hamon and Cresswell (1972) and Golding and Symonds (1978), who reported mesoscale structures with length scales of 200–300 km and 140 km, respectively. He concluded that both length scales can be present with the shorter wavelength ($\lambda = 157 \pm 25$ km) associated with Rossby deformation-scale eddy structures in the strong poleward flow over the slope and the longer ($\lambda = 309 \pm 28$ km) associated with the weaker, large-scale, West Australian Current

TABLE 2. Initial temperature for North West Shelf.

Layer	Temperature (°C)
1	29.5
2	28.5
3	26.0
4	20.5
5	15.7

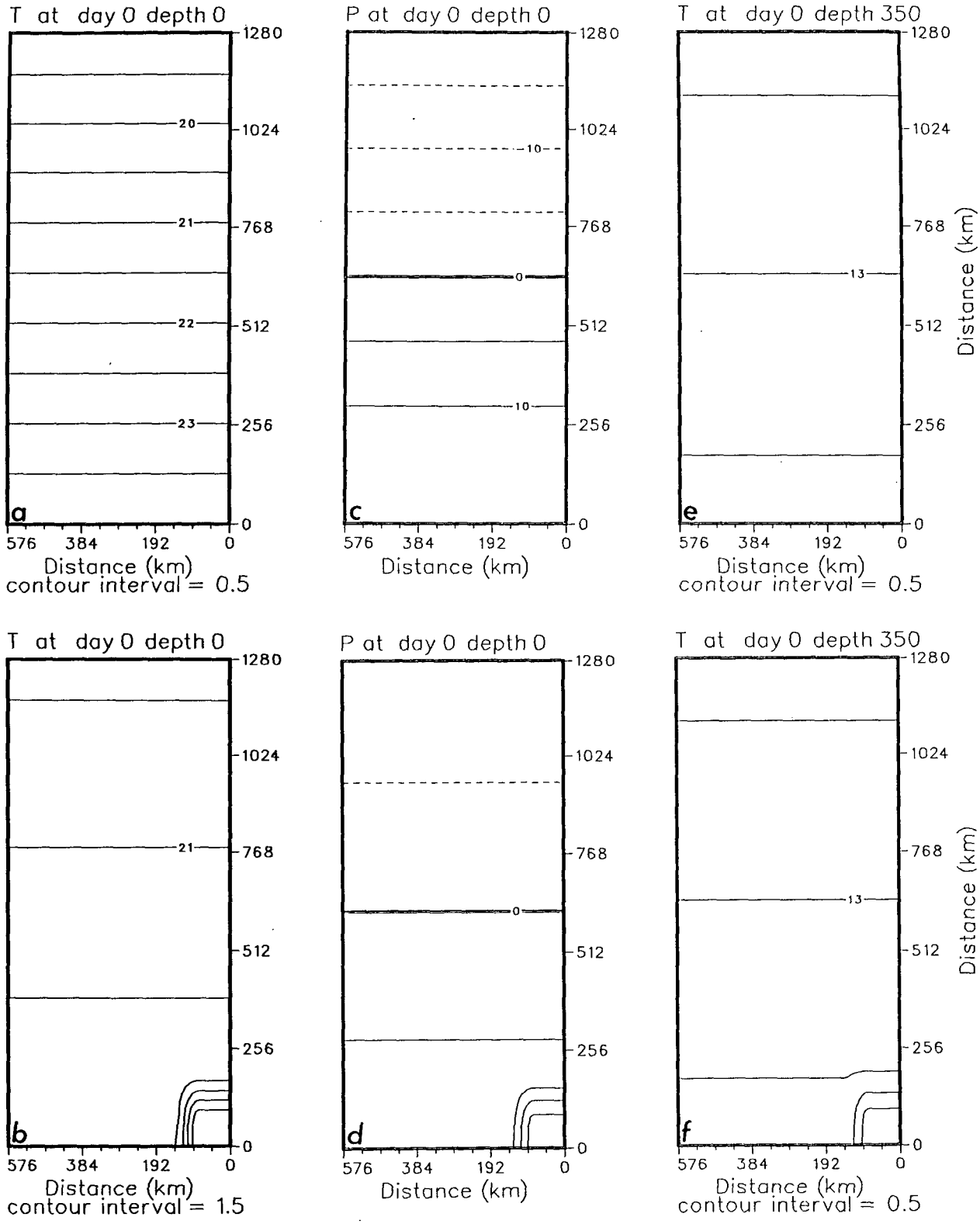

FIG. 2. The initialized fields of surface temperature (T) for Case 1 (a) and Case 2 (b); of surface dynamic height (p) (referenced to 2000 m depth) for Case 1 (c) and Case 2 (d); and of the 350 m depth temperature (T) for Case 1 (e) and Case 2 (f). The model results shown here, and in subsequent plots, have been plotted with a Northern Hemisphere interpretation so that the equatorward (poleward) end of the domain is at 0 km (1280 km) in the alongshore direction. The contour interval is 0.5°C for (a), (e) and (f), 1.5°C for (b), 5 cm for (c), and 10 cm for (d). In all the temperature plots (a,b,e, f), the temperature increases equatorwards.

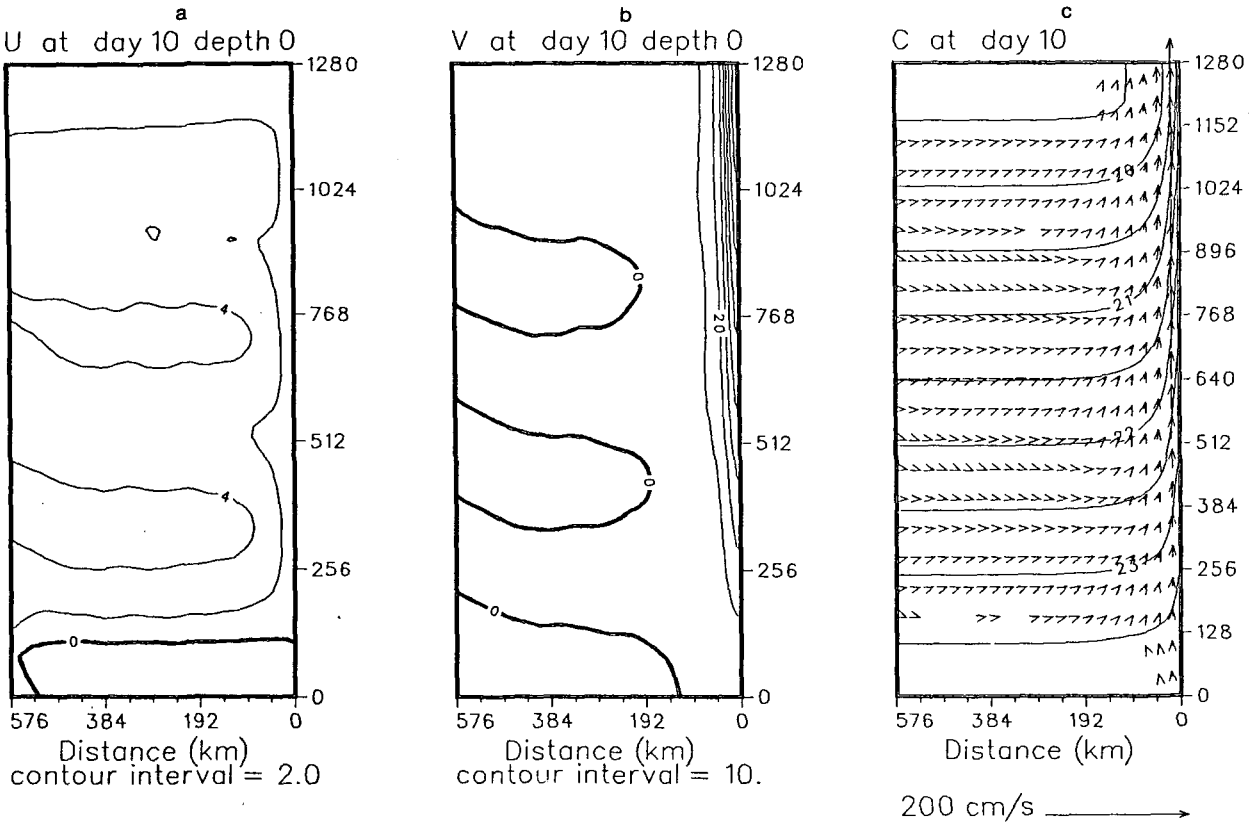

FIG. 3. Time sequence for Case 1 for days 10, 40, 80, 120 and 160 for the surface (a) zonal velocity, (b) meridional velocity, and (c) velocity vector fields superimposed on the temperature fields. The contour interval is 2 cm s^{-1} at days 10, 40, 80, and 5 cm s^{-1} at days 120 and 160 for (a), 10 cm s^{-1} for (b), and 0.5°C for (c). Solid contours denote onshore velocities in (a) and poleward velocities in (b). In all the velocity vector fields presented (Figs. 3c, 5b, 11c and 12b), to avoid clutter, velocity vectors are plotted at every fifth gridpoint in both the cross-shore and alongshore directions, and velocities less than 2 cm s^{-1} for the surface and 1 cm s^{-1} for 350 m depth are not plotted.

offshore. While Andrews (1983) suggested baroclinic instability in the poleward current as a likely generation mechanism, no explanation was offered for the larger offshore scale.

e. *Objective of the study*

Because no modeling studies have successfully produced eddy fields which would allow analysis of their generation mechanisms, the objective of this study is to use a full primitive equation (PE) numerical model to investigate the generation and stability of the Leeuwin Current and eddies. In particular, the roles of the Indian Ocean temperature field and the NW Shelf waters in generating both the current and the eddies will be investigated. In a subsequent study by Batteen and Rutherford (1990), the additional effects of wind forcing on the Leeuwin Current will be considered. The use of a multilevel PE model with active thermodynamics and appropriate choices for diffusion parameters should result in the first modeling study of the Leeuwin Current and its associated eddy fields.

Initializations of the Indian Ocean temperature field and the NW Shelf waters will be similar to those used by Weaver and Middleton (1989). The use of a straight meridional vertical wall for the coastline and the absence of shelf and bottom topography should not severely limit this process-oriented study as the coast is generally straight over the domain (22° to 34°S) and, as Weaver and Middleton note, their modeled current is centered near the shelf break. This study should confirm and extend previous modeling studies and provide a firm basis for further research.

For each thermal forcing mechanism proposed for the Leeuwin Current, we will present the simulated characteristics of the Leeuwin Current and its associated eddy fields and will analyze the results. A comparison of model results with available observations will also be made to assess whether the simulated features of the current and eddies are consistent with those observed. In addition, because no previous studies have focussed on the dynamical reasons for the generation and growth of eddies in and around the Leeuwin Current, we will make an extensive analysis of the gener-

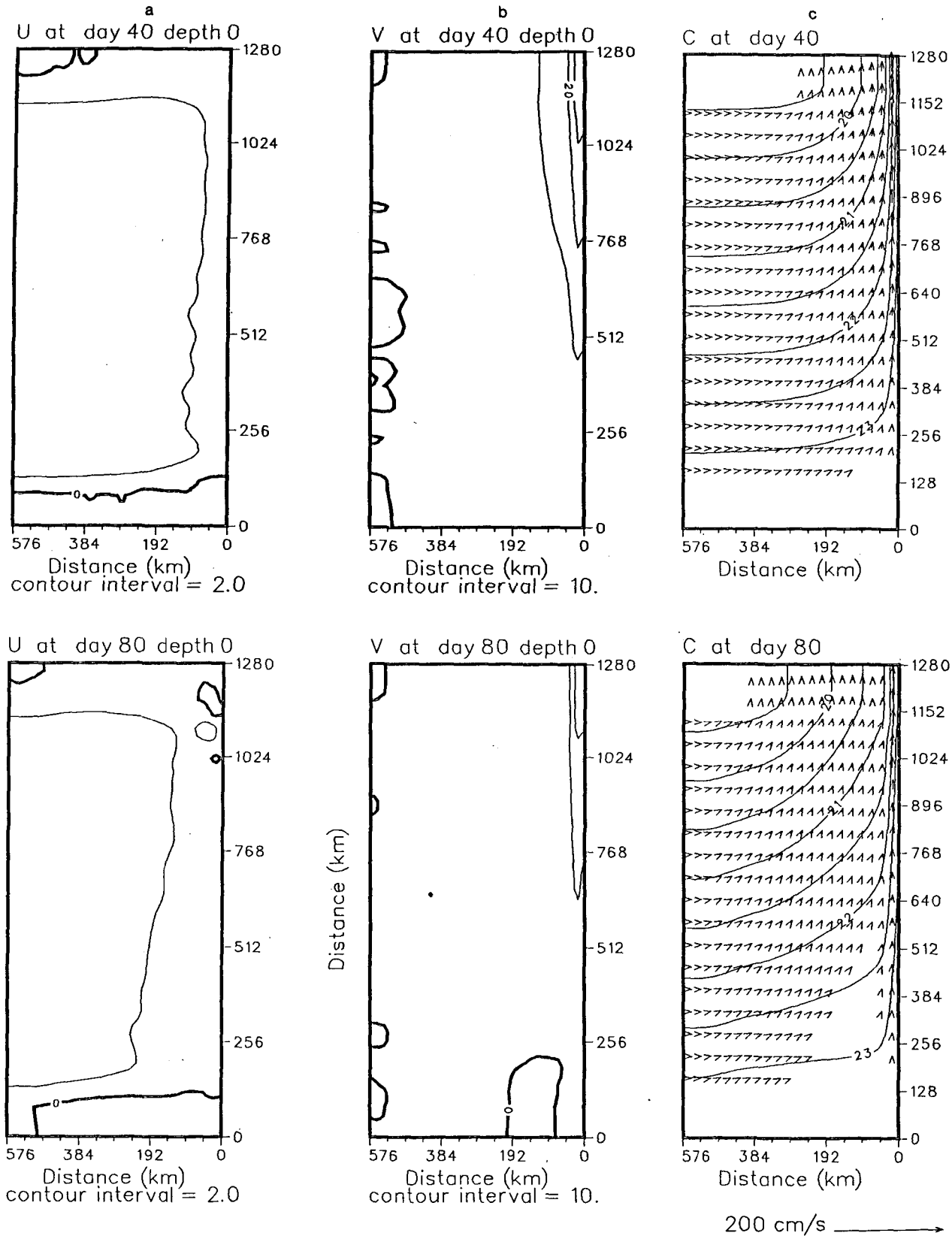

FIG. 3. (*Continued*)

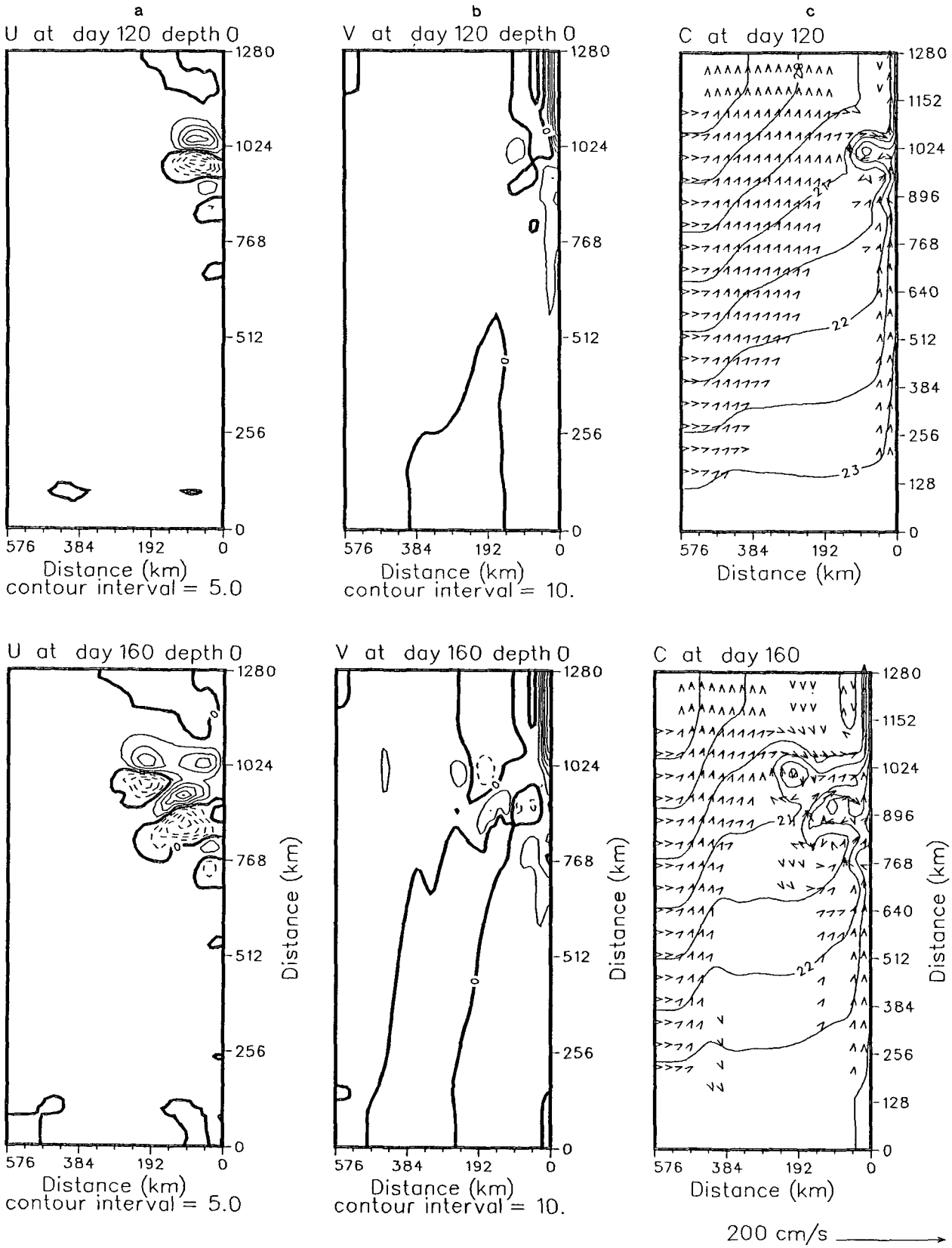

FIG. 3. (*Continued*)

ation mechanisms for the eddies in the Leeuwin Current, using the energy, spectral, and stability techniques described in the Appendix.

The organization of this study is as follows. In section 2 we describe the numerical model and the specific experimental conditions. The results of the numerical experiments are presented in section 3 along with a comparison with observations and an analysis of the generation mechanisms for the Leeuwin Current eddy fields. A summary is presented in section 4.

2. Model description and specific experimental conditions

a. *Model description*

The numerical model used in this study is an adaptation of the model used by Batteen et al. (1989). It is a ten-level PE model for a baroclinic ocean on a β-plane, based on the hydrostatic, Boussinesq, and rigid lid approximations. The governing equations are defined in Batteen et al. (1989). Unlike Batteen et al. (1989), there is no wind forcing used in this study. As described in the next section, the model is initialized with thermal forcing. For the finite differencing, a space-staggered B-scheme (Arakawa and Lamb 1977; Batteen and Han 1981) is used in the horizontal. In the vertical, the ten layers are separated by constant z levels at depths of 13, 46, 98, 182, 316, 529, 870, 1416, 2283 and 3656 m.

The eastern boundary of the model domain represents a straight idealization of the continental shelf off Western Australia (Fig. 1). A no-slip condition on the alongshore velocity is invoked. The northern, southern, and western borders are open boundaries that use a modified version of the radiation boundary conditions of Camerlengo and O'Brien (1980). The model domain is a rectangular area 1280 km alongshore covering latitudes 22° to 34°S, extending 576 km offshore. Horizontal resolution of the model is 20 km alongshore and 9 km cross-shore. Comparisons with numerical simulations made by a higher resolution model (10 km by 9 km) with half the latitudinal extent showed no significant degradation in the resolution of mesoscale features in the coarse grid model; hence, the present grid resolution was adopted to enable coverage of the larger geographical region off Western Australia. Because the model is an adaption of a Northern Hemisphere model, model results will be discussed in terms of alongshore (poleward or equatorward) and cross-shore (onshore or offshore) flows (as in McCreary et al. 1986, who also adapted a Northern Hemisphere model). This use of terminology should facilitate comparison with other eastern boundary currents.

In order to isolate the role of thermal forcing in the generation and stability of the Leeuwin Current and eddies, both coastline features and topography are omitted from this process-oriented study. The inclusion of coastline features and bottom topography, and an examination of their effects on the current and eddies, are considered a separate study. The constant depth used in the model is 4500 m.

Unlike previous Leeuwin Current modeling studies (e.g., McCreary et al. 1986; Weaver and Middleton 1989), which used Laplacian lateral heat and momentum diffusion, the model uses biharmonic lateral heat and momentum diffusion with the same choice of coefficients, i.e., 2.0×10^{17} cm^4 s^{-1} as in Batteen et al. (1989). Holland (1978) showed that the highly scale-selective biharmonic diffusion acts predominantly on sub-mesoscales, while Holland and Batteen (1986) found that baroclinic mesoscale processes can be damped by Laplacian lateral heat diffusion. As a result, the use of biharmonic lateral diffusion should allow mesoscale eddy generation via barotropic and/or baroclinic instability mechanisms. As in Batteen et al. (1989), weak (0.5 cm^2 s^{-1}) vertical eddy viscosities and conductivities are used. Bottom stress is parameterized by a simplified quadratic drag law (Weatherly 1972).

b. *Specific experimental conditions*

The model is initialized with climatological thermal forcing. The ocean is then allowed to geostrophically adjust in the absence of external forcing. The ocean temperature structure used to initialize the experiments is considered in two parts with the warmer, less saline NW Shelf waters separated from the Indian Ocean waters. Climatological mean temperatures for both the Indian Ocean and the NW Shelf are used and zonal homogeneity is assumed in the Indian Ocean. These specific experimental conditions are similar to those used by Weaver and Middleton (1989).

The initial temperature data used for the Indian Ocean are presented in Table 1 for each layer of the model. The temperature data were derived from Levitus (1982). After interpolating between data points, a vertically integrated temperature for each layer was calculated and applied to the constant z levels. For computational ease, the data were further smoothed and a linear gradient fitted to each layer over its meridional extent. Zonal homogeneity was assumed at all levels as the data show little variability, apart from in the region of the Leeuwin Current. Slight differences between the final values used for the Indian Ocean forcing in this study (Table 1) and those of Weaver and Middleton (1989) (the same Levitus data source was used) could be due to slightly different vertical integration and smoothing techniques and/or to the additional data sources of Rochford (1962, 1969) used by Weaver and Middleton (1989).

Salinity values from Levitus (1982) have a range of only 35.6 $\pm$ 0.2 ppt over most of the domain in the upper five layers. This range is considered narrow enough to discount salinity variability, so that no com-

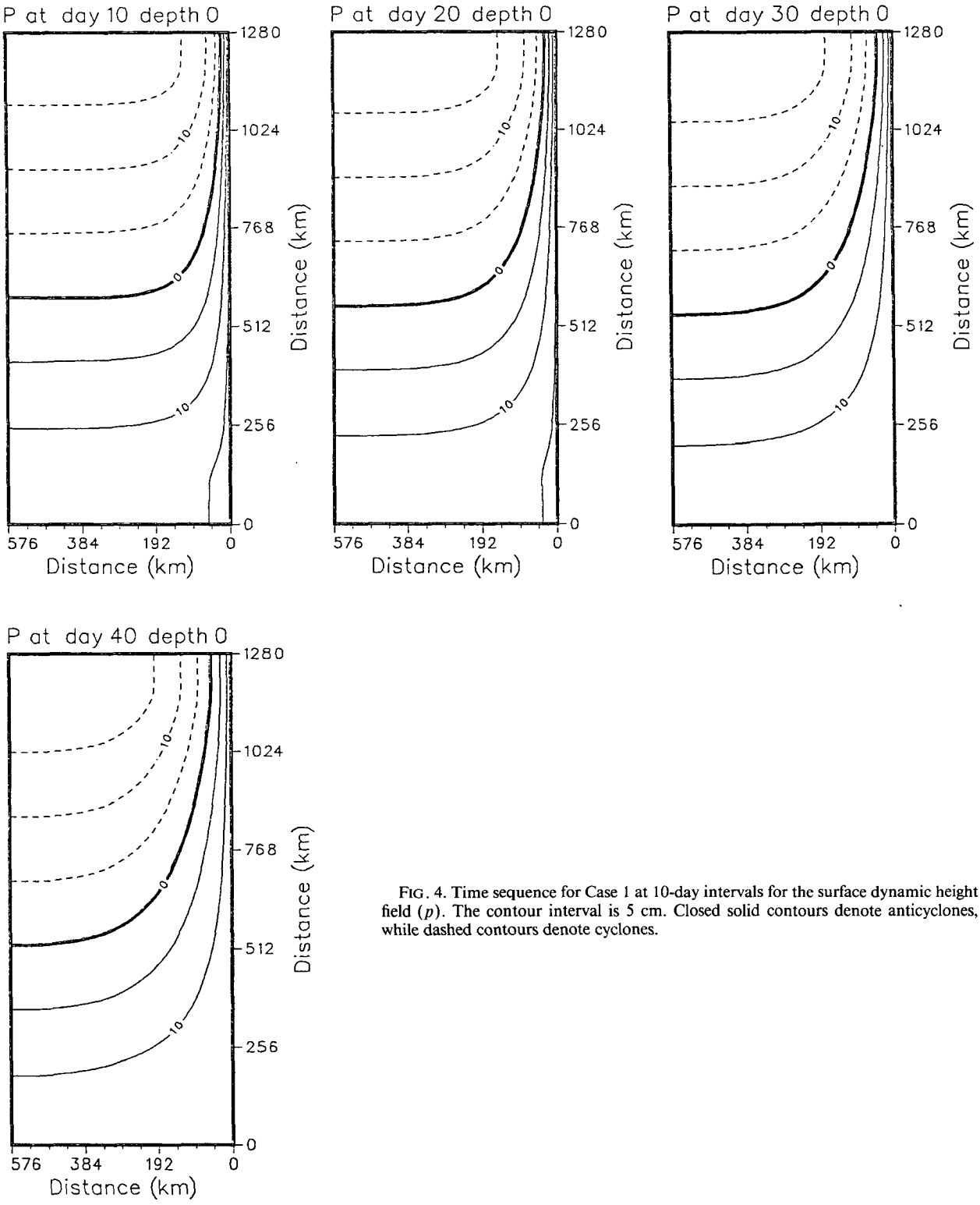

FIG. 4. Time sequence for Case 1 at 10-day intervals for the surface dynamic height field (p). The contour interval is 5 cm. Closed solid contours denote anticyclones, while dashed contours denote cyclones.

pensation is made for the assumption that density is a function of temperature alone.

To investigate the impact of NW Shelf waters separately from the Indian Ocean, the NW Shelf waters are initialized separately in this model. As for the Indian Ocean, the data were again derived from Levitus (1982)

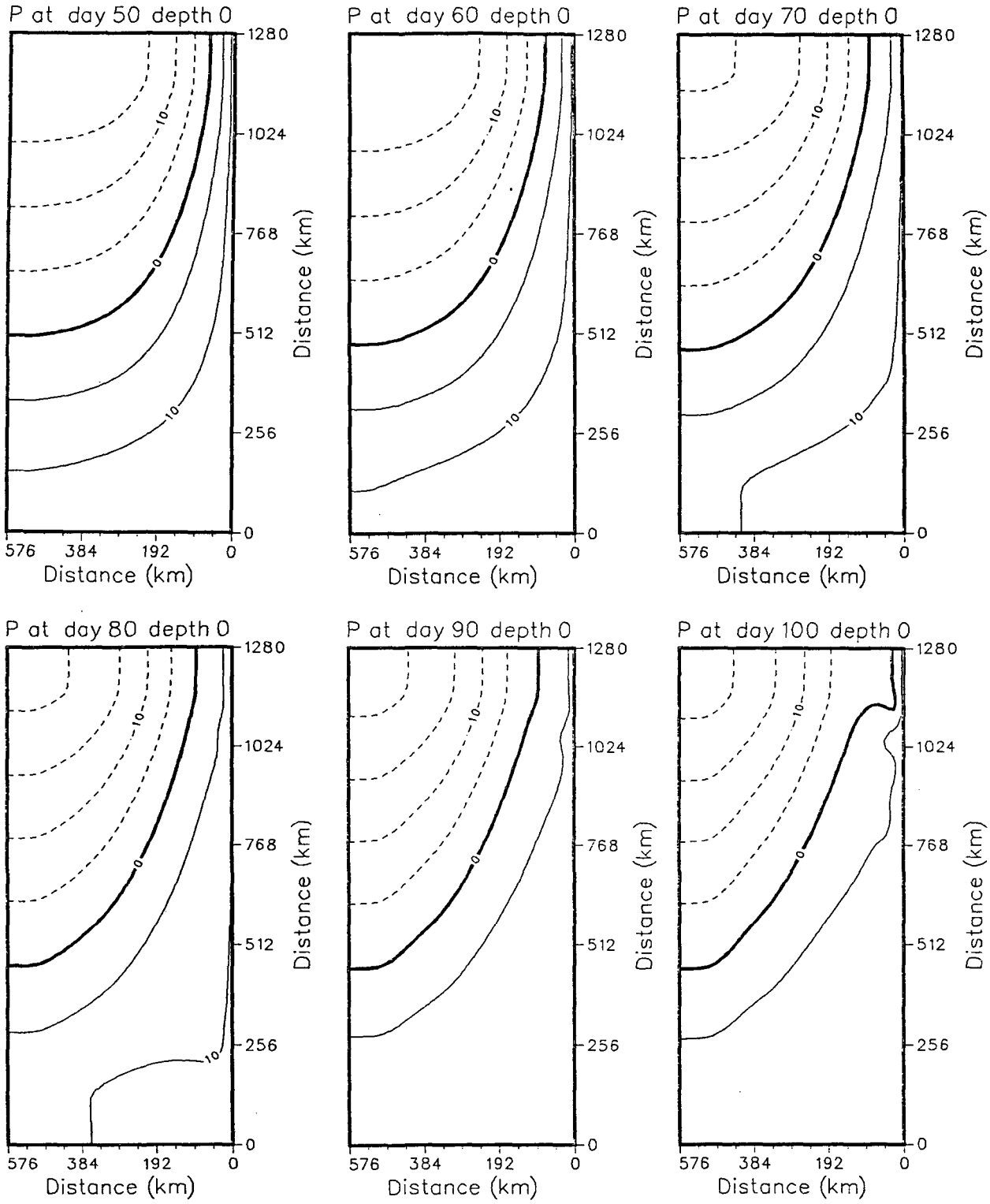

FIG. 4. (*Continued*)

and vertically integrated and smoothed. Due to the marked contrast in salinity between the water masses of the Indian Ocean and the NW Shelf, the NW Shelf waters are given an equivalent temperature that compensates for variations from a mean salinity of 35.6 ppt.

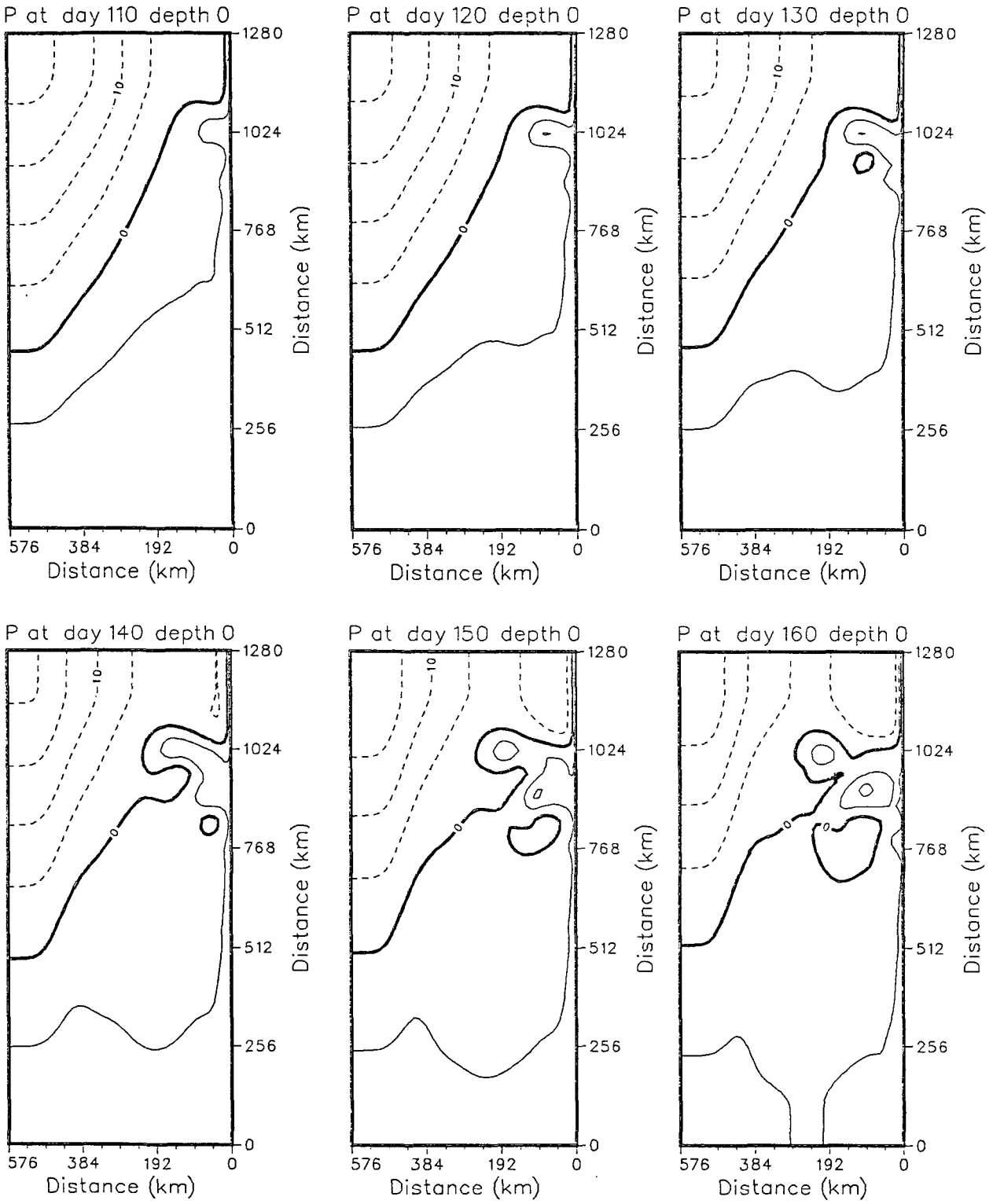

FIG. 4. (*Continued*)

The NW Shelf waters are restricted to the upper five layers only, so that the lower layers are initialized as for the Indian Ocean. When included in the experiments, the NW Shelf waters are treated as a raft of warm water in the inshore equatorward end of the model, in the upper 500 m and are linearly smoothed

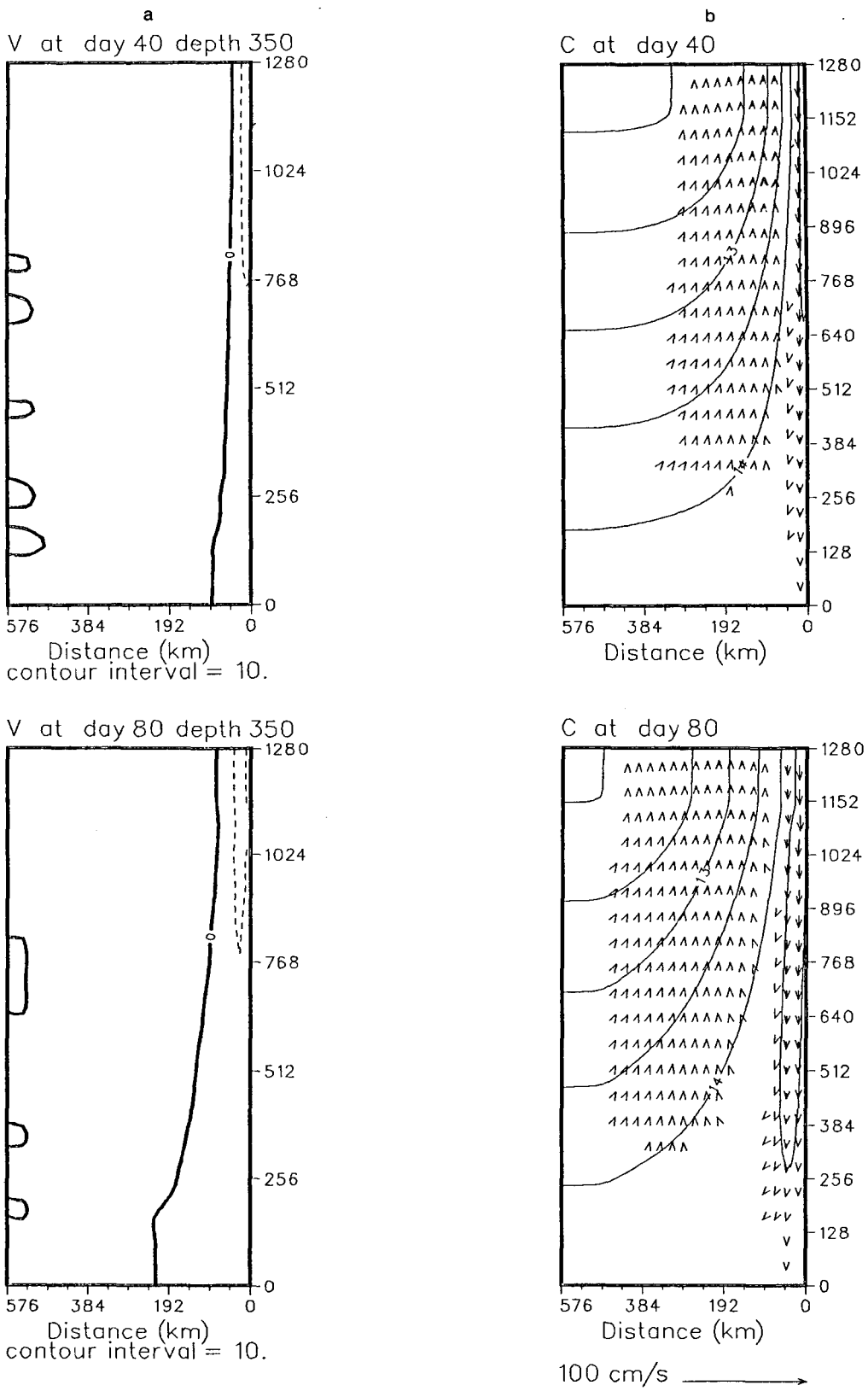

FIG. 5. Time sequence for Case 1 at 40-day intervals at 350 m depth for (a) meridional velocity and (b) velocity vector fields superimposed on the temperature fields. The contour interval is 10 cm s^{-1} for (a), and 0.5°C for (b).

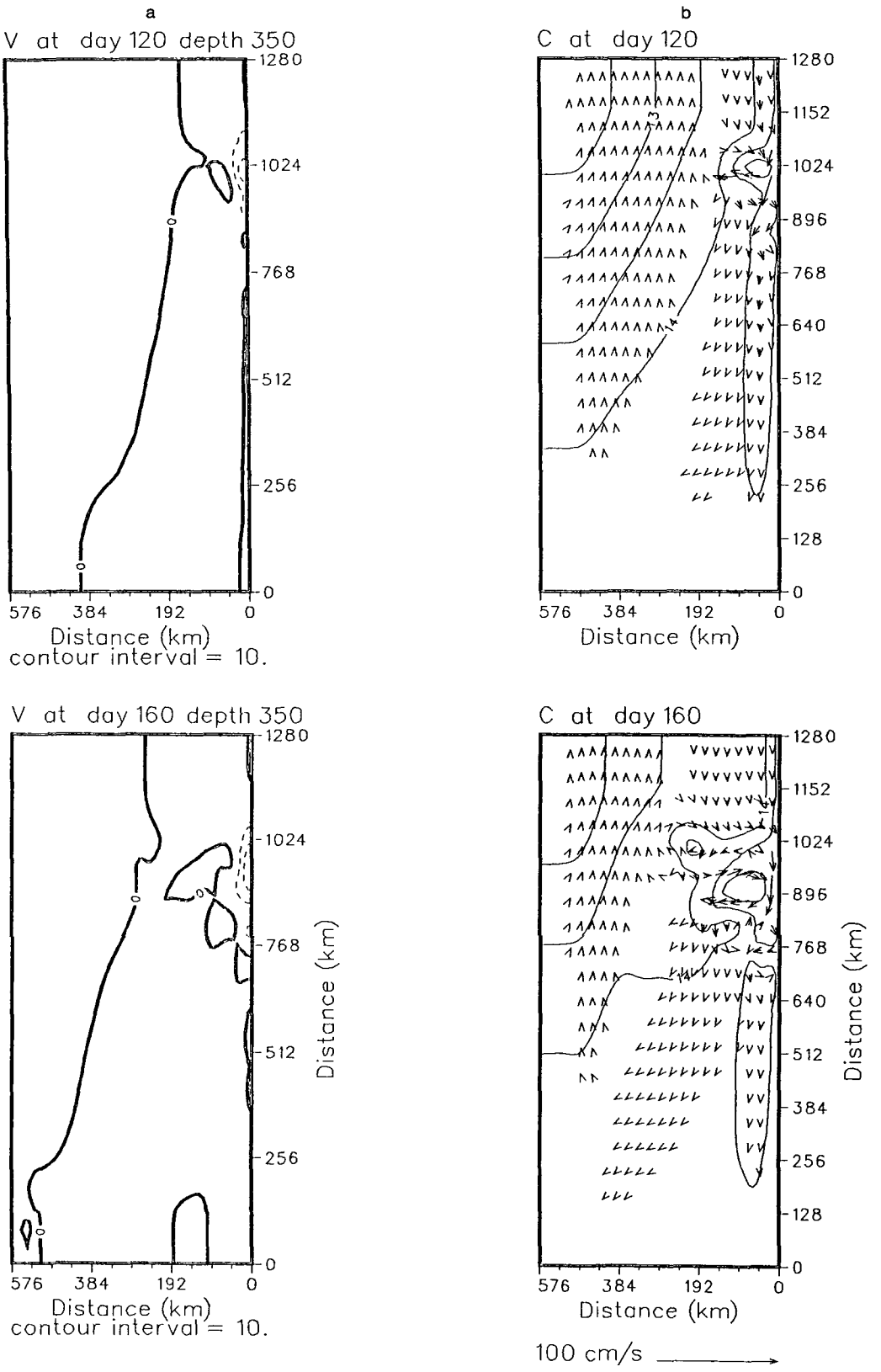

FIG. 5. (*Continued*)

into the surrounding Indian Ocean waters. The values used to initialize the NW Shelf waters are presented in Table 2.

The first of the forcing mechanisms to be investigated is the Indian Ocean thermal gradient. In this experiment, hereafter referred to as Case 1, the model is initialized with the temperature data from Table 1 and allowed to run for 160 days. This time period was chosen to include both the generation of the current and any eddies which may form in the flow.

In the second experiment, hereafter referred to as Case 2, the role of the NW Shelf waters is investigated. The background Indian Ocean thermal field is retained to maintain the large-scale forcing as in Case 1. The warmer water, as detailed in Table 2, is then added to the inshore, equatorward corner of the model to simulate the influx of NW Shelf waters. The model is then run for 160 days.

3. Results of the numerical experiments

a. Case 1. Forcing by Indian Ocean density field

1) GENERATION OF THE CURRENTS AND EDDIES

The initialized surface thermal and dynamic height fields are shown in Figs. 2a and c, respectively. A time sequence of the fields of surface cross-shore (u) and alongshore (v) velocity components and of the velocity vectors (**c**) superimposed on the temperature field is shown in Fig. 3, and of the surface dynamic height (p) field (calculated from a reference level of 2000 m) in Fig. 4.

(i) *Pre-eddy period (days 0–80)*

As expected, when the temperature decreases poleward (Fig. 2a), the pressure gradient due to the temperature gradient establishes an onshore geostrophic inflow in the interior ocean (Figs. 3a,c). Because the initialized alongshore temperature field is not constant, the onshore flow varies between 2 and 5 cm s^{-1}. On approaching the eastern boundary, the onshore flow turns and forms a poleward flowing boundary current (Figs. 3b,c), which advects warm water from the equatorial end of the domain (Fig. 3c). Because it is continually augmented downstream by additional onshore flow, the poleward current increases in magnitude toward the pole, so that by day 10 maximum velocities of the order of 70 cm s^{-1} are observed near the poleward end of the domain (Fig. 3b). As time progresses, the onshore geostrophic flow weakens slightly in magnitude to between 2 and 3 cm s^{-1} (Fig. 3a) so the geostrophic process slows down. The poleward boundary current significantly weakens as time progresses so that maximum speeds decrease from 50 cm s^{-1} at day 20 (not shown) to 30 cm s^{-1} at day 40 (Fig. 3b). A minimum speed of 20 cm s^{-1} is reached by day 50, and is maintained through day 80 (Fig. 3b).

The 10-day time sequence of the dynamic height field (Figs. 2c and 4) for this time period shows that, as expected, by day 10 there is an increase in dynamic height near the coast, which is maintained throughout the experiment. Also at day 10, due to the strong poleward velocity, there is a tight dynamic height gradient at the poleward end of the domain. From days 20–70, the gradient widens with time, consistent with the weakening of the poleward current. Likewise, due to the slowing down of the geostrophic process with time, the initially strong onshore flow is seen to dissipate westward.

The v and **c** fields for 350 m depth, corresponding to the average core depth of the undercurrent (see Fig. 10b), are presented for this time period in Figs. 5a and 5b, respectively. The initial thermal field is shown in Fig. 2e. By day 40 (Figs. 5a,b), the pressure gradient in the Indian Ocean due to the thermal gradient is sufficient to establish an equatorward flow. The strongest equatorward flow (10 cm s^{-1}) is in the poleward end of the domain and is maintained throughout.

(ii) *Eddy generation period (days 80–160)*

The pressure gradient in the Indian Ocean due to the thermal gradient is sufficient to establish an unstable poleward flow. The u velocity fields (Fig. 3a) are generally the best indicators of eddy formation. By day 80, instability has led to the generation of an eddy at the poleward end of the domain. The eddy growth is seen at day 120 (Figs. 3a,c) and by day 160, the eddies have started to move offshore (Figs. 3a,c) advecting the warm surface temperatures (Fig. 3c) with them.

The 10-day time sequence of the dynamic height field for this time period (Fig. 4) illustrates the evolution of the eddy fields. By day 90 an anticyclonic meander develops at the poleward end of the model domain ($y \sim 1024$ km) on the offshore side of the current. This anticyclonic eddy intensifies and propagates westward with time. From days 130 to 160, other eddies develop equatorward of this eddy, and subsequently intensify and propagate westward with time.

The fields of velocity vectors (**c**) superimposed on the temperature fields at the surface (Fig. 3c) and at 350 m depth (Fig. 5b) illustrate that, away from the eddy generation region, the flow is predominantly parallel to the isotherms, as expected. In the eddy generation region—i.e., in the poleward end of the domain—there is significant advection of warm water offshore by the anticyclonic eddies.

(iii) *Comparisons with other studies*

Overall, the magnitudes of the model poleward (5–40 cm s^{-1}) and equatorward (5–10 cm s^{-1}) currents

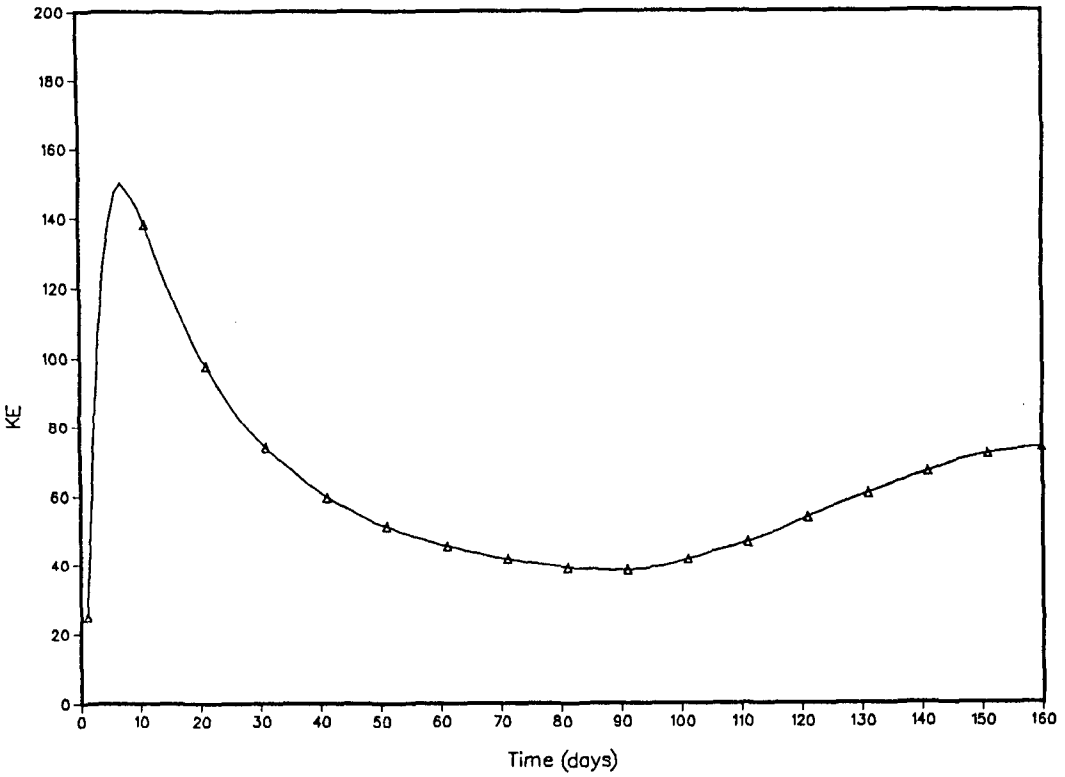

FIG. 6. Energy time series for Case 1 summed over all layers and over the entire domain for total kinetic energy in units of $cm^2 s^{-2}$.

compare favorably with observations taken near the poleward end of the current during the austral winter. In particular, the current magnitudes are consistent with the current meter data obtained at Cape Mentelle (34°S) in LUCIE (Boland et al. 1988), which show mean alongshore poleward velocities of 28.8 cm s^{-1} at 43 m depth, decreasing to 3.2 cm s^{-1} at 230 m depth, with evidence of an undercurrent at 320 m depth. However, comparisons with the LUCIE current meter observations at the equatorward end of the domain show that the alongshore velocities produced by the model may be too weak. For example, the current meter data obtained at Carnarvon (25°S) show mean poleward velocities of 5.7 cm s^{-1}, while the model results show mean velocities of 1.5 cm s^{-1} at the same location and depth. Since the current meter data at Carnarvon are located on a sloping shelf, it may well be that the model underestimates the alongshore velocities in this region, since the inclusion of a sloping shelf in a model can increase the magnitude of the alongshore current (Weaver and Middleton 1989). However, as Case 2 will show, the NW Shelf waters augment the poleward velocities in the equatorward end of the domain, so that a sloping shelf may not be required to obtain comparable alongshore velocities.

Consistent with the buoy observations of Cresswell and Golding (1979, 1980), eddies form in the horizontal shear zone on the offshore side of the current. The anticyclonic, westward-propagating eddy at the poleward end of the model domain ($y \sim 1024$ km) is reminiscent of observations by Cresswell and Golding (1979) and Godfrey et al. (1979) of a semipermanent anticyclonic eddy located west of Cape Naturaliste (33.5°S). [According to Godfrey (personal communication, 1990), since it is primarily the anticyclonic, warm core eddies that have been observed to move offshore, this could result in a selective way of weakening both temperature and steric height gradients off Western Australia.]

The model results are also consistent with those of previous modeling studies, e.g., McCreary et al. (1986) and Weaver and Middleton (1989). In particular, the general structure of the Leeuwin Current is portrayed, with a poleward surface current overlying an equatorward undercurrent (see Fig. 10b). The undercurrent rises as it flows equatorward and weakens in intensity (Fig. 5). The surface current is augmented by onshore geostrophic inflow and accelerates downstream. Consistent with Weaver and Middleton (1989), after the surface current reaches its largest velocity, it subsequently broadens and drifts westward through baroclinic Rossby wave propagation. After about 80 days the surface current at the poleward end of the domain intensifies again (Fig. 3b), which, consistent with

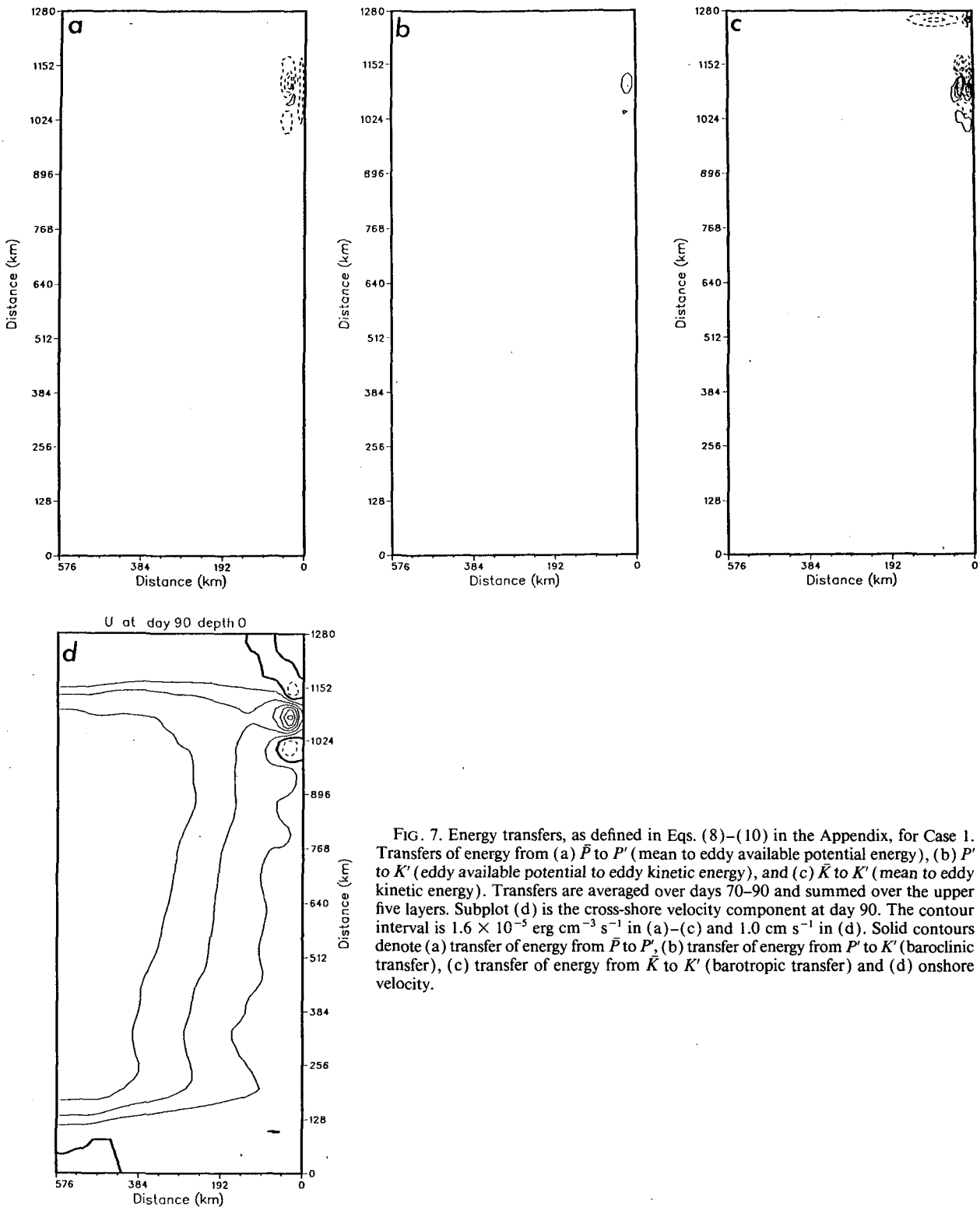

FIG. 7. Energy transfers, as defined in Eqs. (8)–(10) in the Appendix, for Case 1. Transfers of energy from (a) $\bar{P}$ to P' (mean to eddy available potential energy), (b) P' to K' (eddy available potential to eddy kinetic energy), and (c) $\bar{K}$ to K' (mean to eddy kinetic energy). Transfers are averaged over days 70–90 and summed over the upper five layers. Subplot (d) is the cross-shore velocity component at day 90. The contour interval is 1.6×10^{-5} erg cm^{-3} s^{-1} in (a)–(c) and 1.0 cm s^{-1} in (d). Solid contours denote (a) transfer of energy from $\bar{P}$ to P', (b) transfer of energy from P' to K' (baroclinic transfer), (c) transfer of energy from $\bar{K}$ to K' (barotropic transfer) and (d) onshore velocity.

Weaver and Middleton (1989), is due to a nonlinear feedback mechanism which becomes important at this time. In particular, the strong offshore fronts, caused by the initial poleward advection, generate thermal winds that feed back to enhance the poleward flow at the surface.

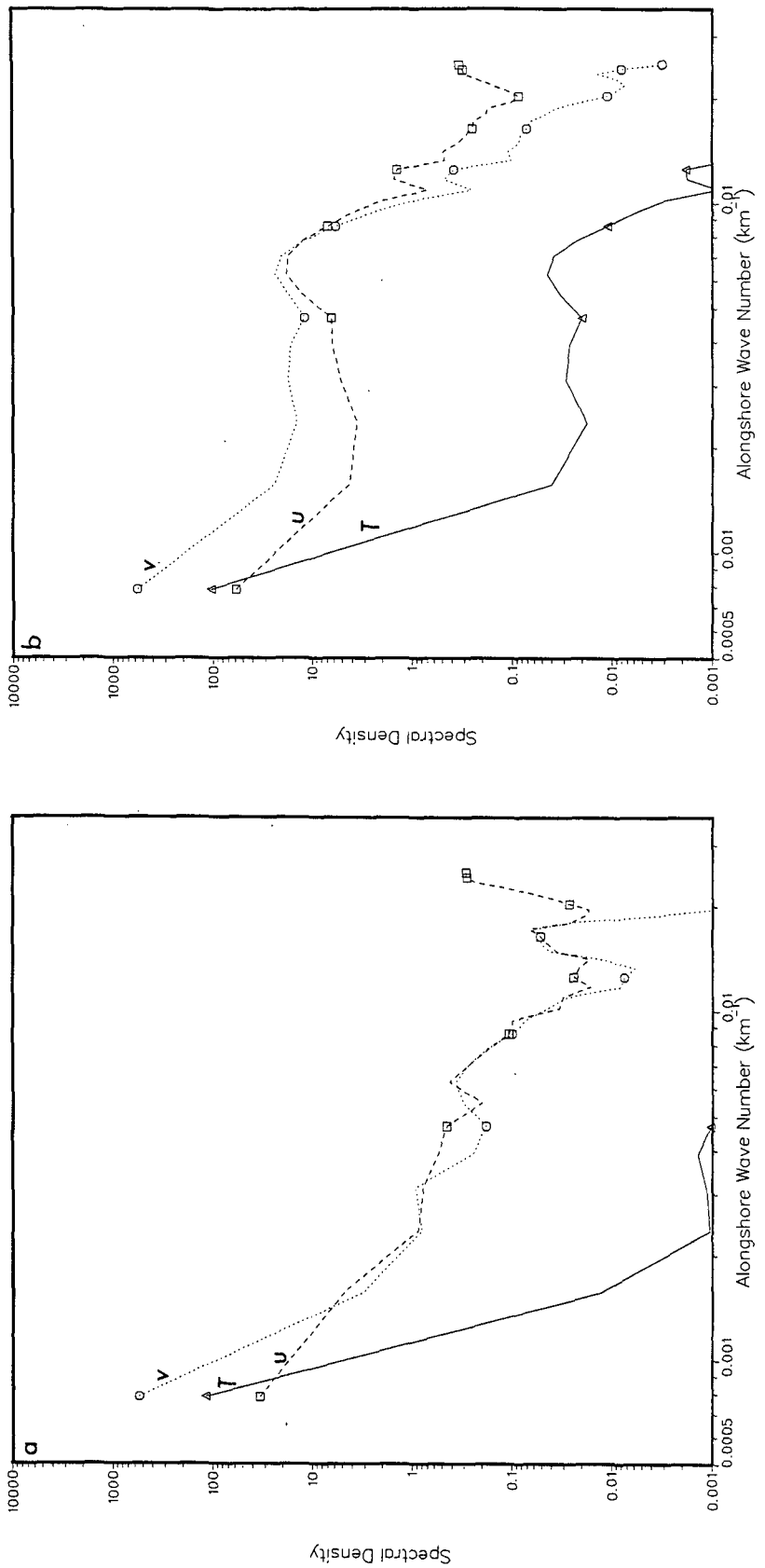

FIG. 8. Spectral density (cm^2 s^{-2} km for u, v; K^2 km for T) versus alongshore wavenumber for Case 1 at days 70 (a) and 100 (b). The wavenumber is an inverse wavelength. A logarithmic scale is used for the spectral density.

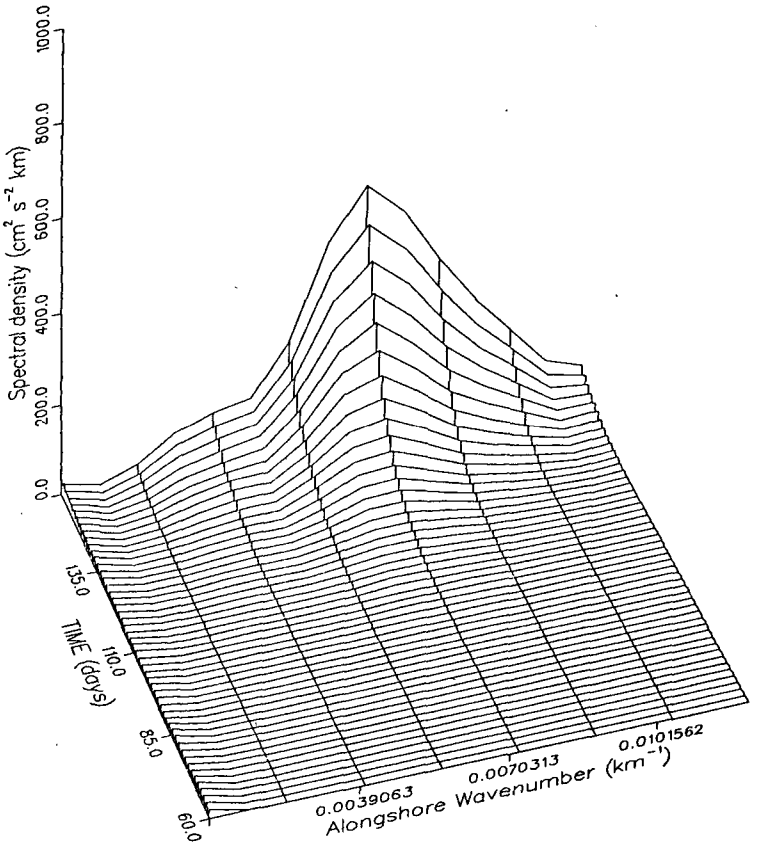

FIG. 9. Time series of spectral density ($cm^2\ s^{-2}\ km$) for u of Case 1 from days 60–160 for the domain extending to 90 km offshore. The amplitude of the spectral energy has been plotted on a linear scale.

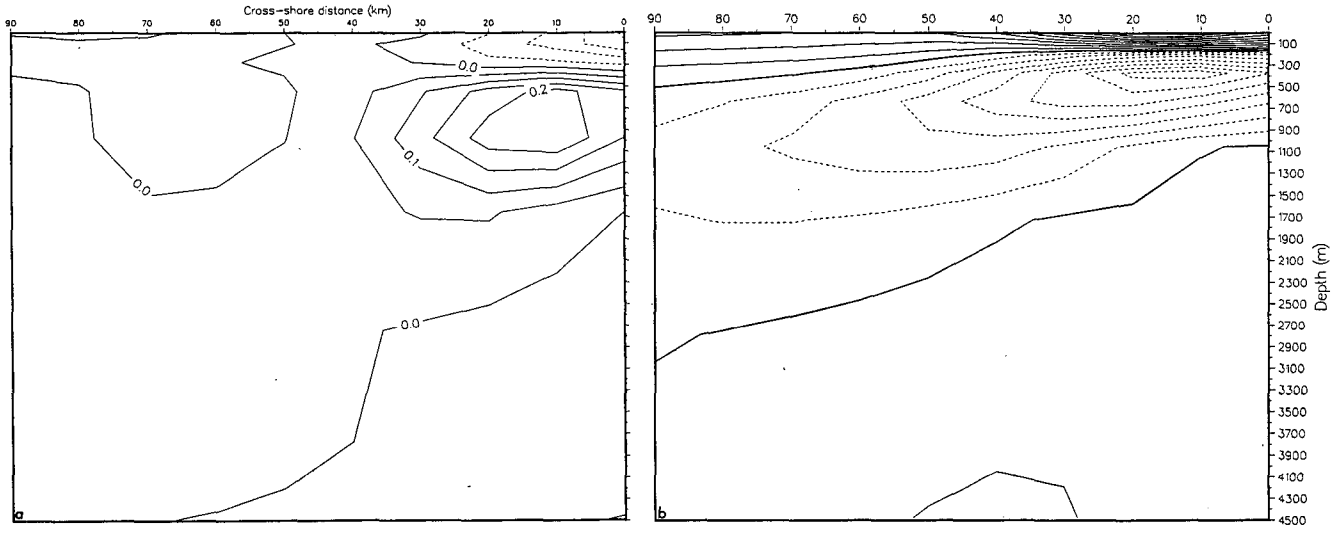

FIG. 10. Cross sections for Case 1 of the alongshore velocity and of the cross-stream derivative of potential vorticity, dq/dx, where q is the potential vorticity defined in Eq. (11) in the Appendix. (a) Vertical cross section of the time-averaged (days 70–90) cross-stream derivative of potential vorticity, multiplied by the grid size ($°C\ m^{-1}\ s^{-1}$), and scaled by 10^8. Contour interval is $0.05°C\ m^{-1}\ s^{-1}$. (b) Vertical cross section of the time-averaged (days 70–90) alongshore velocity component ($cm\ s^{-1}$). Contour interval is 2.0 $cm\ s^{-1}$. Vertical cross sections are at 1080 km alongshore, extending to 90 km offshore. Dashed contours denote negative values.

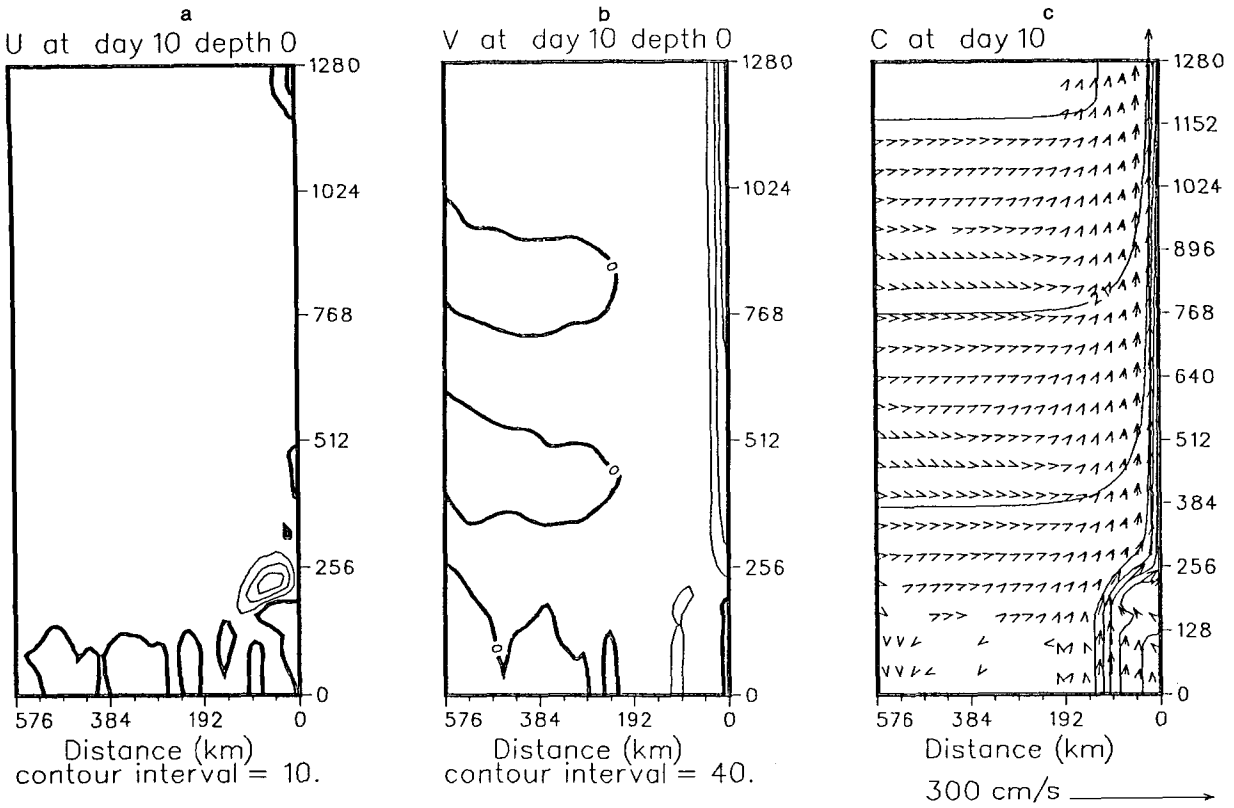

FIG. 11. Same as Fig. 3 but for Case 2. The contour interval is 10 cm s^{-1} for (a), 40 cm s^{-1} for (b), and 1.5°C for (c).

2) ANALYSES OF EDDY GENERATION MECHANISMS

Because no previous studies have focussed on the dynamical reasons for the generation and stability of the eddies in and around the Leeuwin Current off Western Australia, we will make an extensive analysis of the generation mechanisms in Case 1 using the energy, spectral, and stability analyses described in the Appendix. From the energy transfer analysis, the location and magnitude of baroclinic and barotropic transfers can be found. Those waves which are unstable and, in particular, the fastest growing wave, can be determined from the internal Rossby radii, and the spectra can confirm whether those waves could exist.

(i) *Energy analysis*

The energy analysis can be used to determine the temporal mean and eddy kinetic energy and available potential energy from statistics collected during periods of near-constant total energy. Plots of the energy transfers during these periods give the dominant transfers and the regions in which they are most active. The total kinetic energy (Fig. 6) and available potential energy (not shown) over the entire domain and for all layers were plotted in a time series and showed that the available potential energy decreased steadily throughout, whereas the kinetic energy—initially large while the model adjusts geostrophically to the forcing—was nearly steady from days 70 to 90. Because this corresponds to the period of eddy generation, the energy transfers are calculated for that period.

Analysis of horizontal plots of the energy transfers can be used to find the location and magnitude of baroclinic and barotropic transfers. Figure 7 shows horizontal plots for (a) the transfer between mean and eddy available potential energy, (b) baroclinic transfer, and (c) barotropic transfer for the period days 70–90. Also shown, in Fig. 7d, is the cross-shore velocity component at day 90. The transfers are clearly strongest in the region of the eddy development. A comparison of plots 7b and 7c, which have the same contour interval, indicates that barotropic instability is more important than baroclinic instability in providing the eddy kinetic energy. The magnitude of the transfers was calculated for a subdomain centered on the position of the eddy at day 90, and showed barotropic instability to be stronger than baroclinic in the immediate vicinity of the eddy development.

(ii) *Spectral analysis*

Figures 8a and 8b show the spectral density as a function of alongshore wavenumber for days 70 and 100, respectively. A comparison of the two figures shows energy increasing at a wavelength near 150 km (alongshore wavenumber of ~0.0065 km^{-1}) during this period of eddy development (i.e., days 70–100). Figure 9 shows the time series of spectral density from

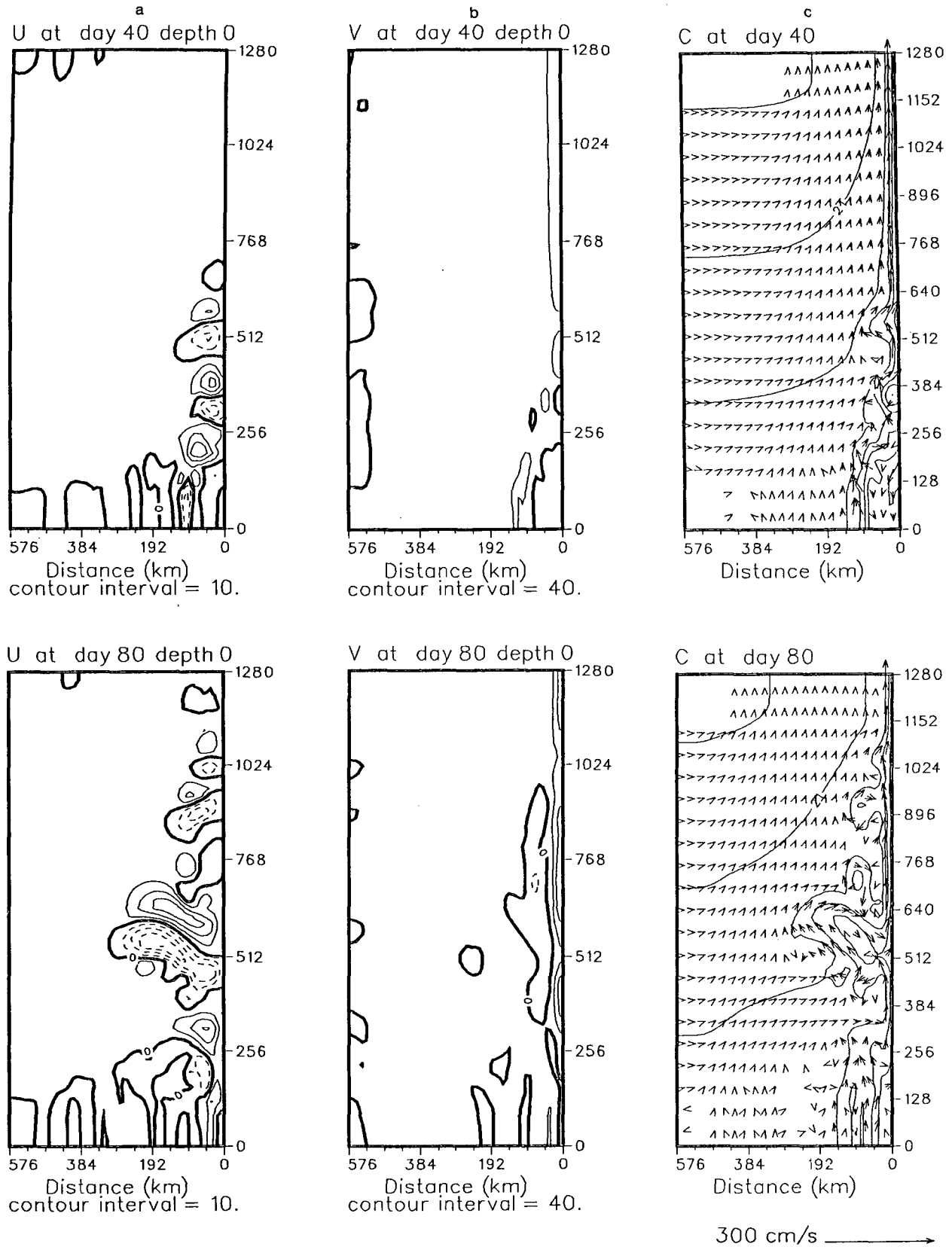

FIG. 11. (*Continued*)

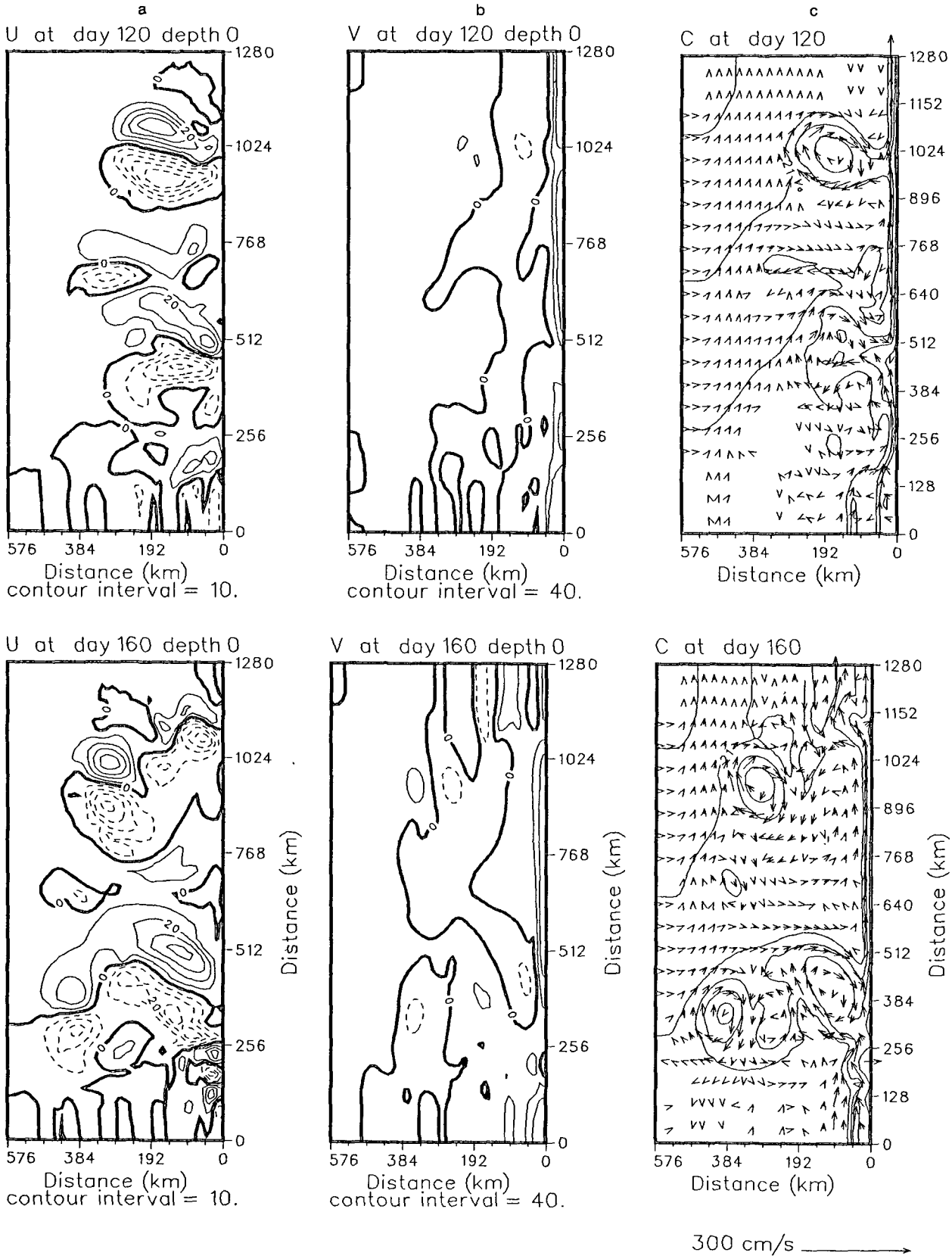

FIG. 11. (*Continued*)

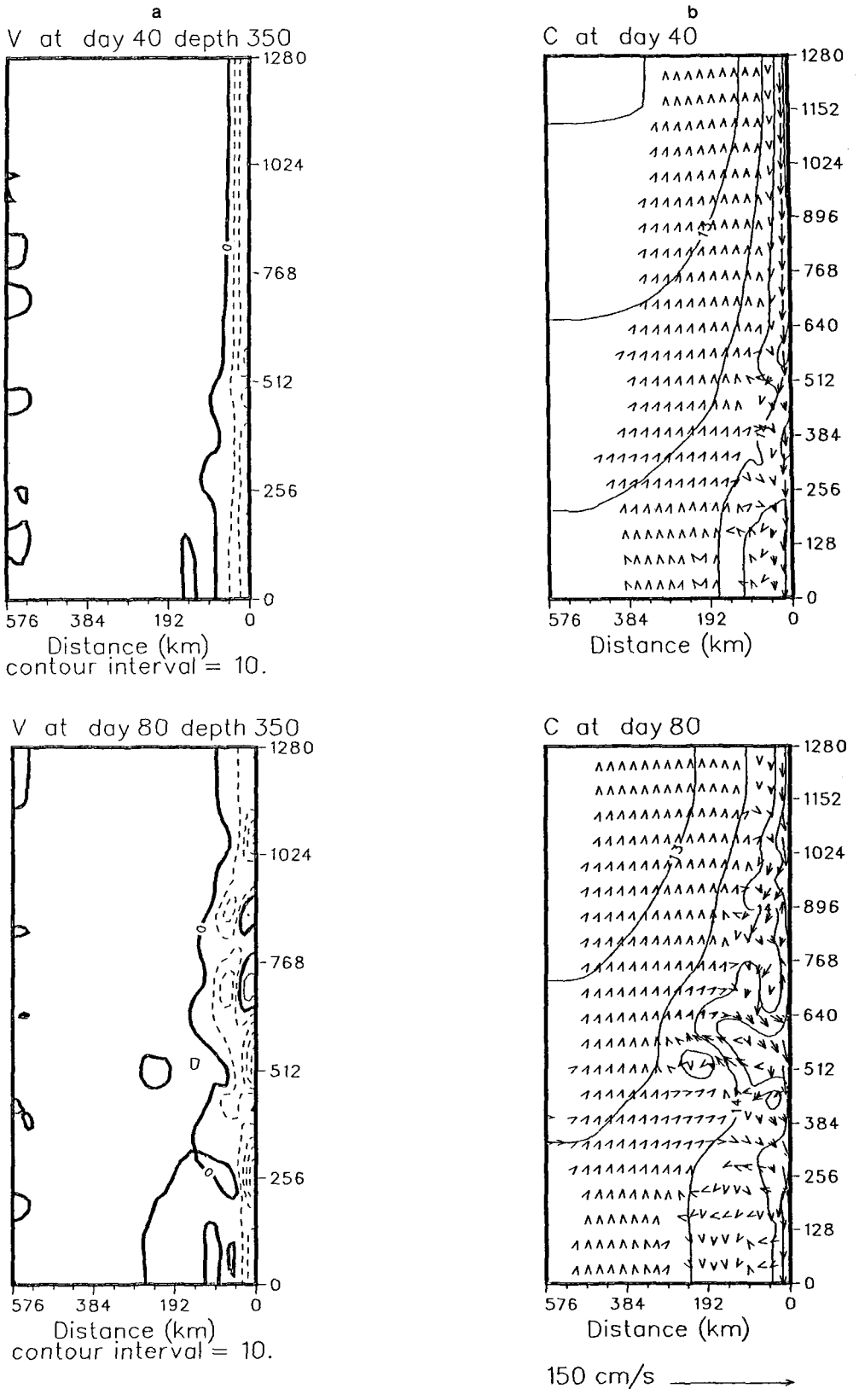

FIG. 12. Same as Fig. 5 but for Case 2. The contour interval is 10 cm s^{-1} for (a) and 0.5°C for (b).

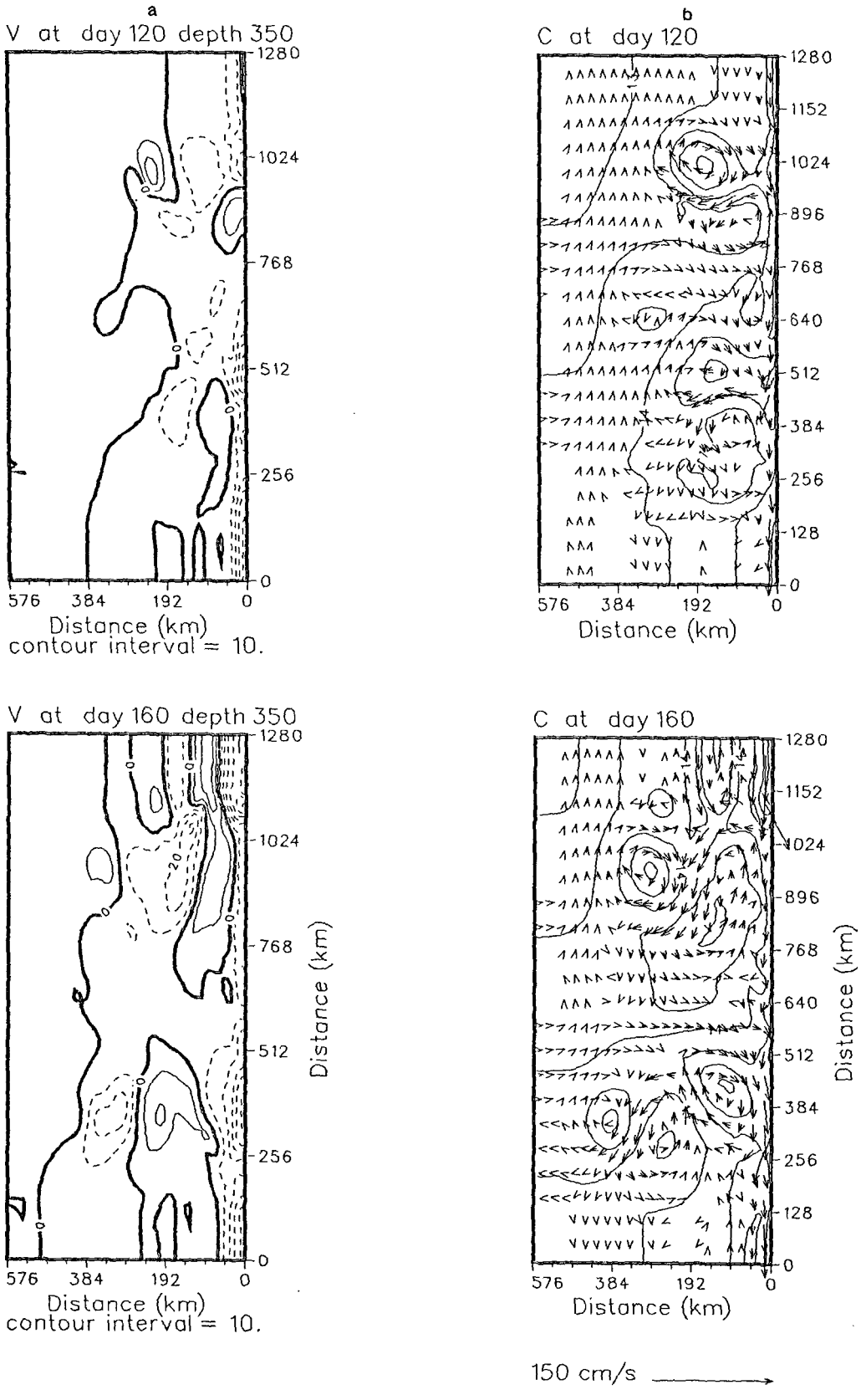

FIG. 12. (*Continued*)

days 60 to 160. Note that, because the amplitude of the spectral energy is on a linear scale, the aspect of this type of plot makes it possible for peaks to "hide" other features; i.e., the linear amplitude scale can suppress all but the dominant wavenumbers. While the initial development is not apparent in the 160 day spectral time series for Case 1 (Fig. 9), the peak energy at the end of the experiment is also at a wavelength near 150 km. Hence, both development and subsequent growth of eddies appear to be at the same wavelength scale.

(iii) *Instability analysis*

Finally, the necessary and sufficient conditions for the sources of instability are investigated. Figure 10a shows the alongshore and time-averaged horizontal gradient of potential vorticity and Fig. 10b the alongshore and time-averaged alongshore velocity. Both are averaged over the model's entire meridional extent and over days 70–90. The cross-stream derivative of potential vorticity changes sign at several locations and its product with the alongshore mean flow is positive in the domain, satisfying the necessary conditions for baroclinic instability. The necessary conditions for an energy source for instability are satisfied by both the vertical and horizontal shears in the flow.

The internal Rossby radius of deformation, R_d, was calculated for the region of initial instability as 27.6 km. As baroclinic instability favors wave growth at $2\pi R_d$ and barotropic growth at a shorter scale (Kamenkovich et al. 1986), the dominant wavelength scale of ~150 km is consistent with the mixed instability observed in this case.

(iv) *Conclusions*

The poleward surface flow and equatorward undercurrent driven by the Indian Ocean climatological temperature field are unstable and generate mesoscale eddies at the poleward end of the domain. In this region, instability is mixed, with barotropic dominant. The primarily anticyclonic eddies form in the horizontal shear zone on the offshore side of the core of the current, consistent with the buoy observations of Cresswell and Golding (1979, 1980). The eddies have a dominant wavelength of around 150 km, a scale consistent with the Rossby radius of deformation of 27.6 km and the mixed instability mechanism. This wavelength falls within the range of the Rossby deformation length scale of eddies (wavelength $\lambda = 157 \pm 25$ km) noted in the strong poleward flow over the slope by Andrews (1983), and is close to the 140 km length scale of eddies observed by Golding and Symonds (1978).

b. Case 2. Forcing by Indian Ocean and NW Shelf

1) GENERATION OF THE CURRENTS AND EDDIES

The fields of surface cross-shore (u) and alongshore (v) velocity components, and current velocity ($\mathbf{c}$) superimposed on the temperature (T) field are presented in Fig. 11. Figures 2b and 2d show the initialization of the NW Shelf waters (at the inshore equatorward corner), which has been added to the same alongshore temperature gradient of the Indian Ocean used in Case 1.

(i) *Generation of the currents*

As seen in the v and $\mathbf{c}$ fields at day 10 (Figs. 11b and 11c), the inclusion of the NW Shelf waters dominates in the NW Shelf equatorial source region, as expected. Although the effects of the NW Shelf waters weaken away from the source region, they are sufficient to establish a stronger poleward flow than in Case 1, not only in the poleward end of the model domain, where velocities exceed 140 cm s^{-1} (Fig. 11b) but along the entire coastal boundary. The advection of the warmer NW Shelf waters can be seen in the T and $\mathbf{c}$ fields (Fig. 11c) with a narrow core of warm water evident along the coastal boundary. As in Case 1, the poleward boundary current, due to a slowdown of the geostrophic adjustment process and to westward Rossby wave propagation, significantly broadens and weakens as time progresses so that maximum speeds in the poleward end of the domain decrease from 100 cm s^{-1} at day 20 (not shown) to a minimum of 40 cm s^{-1} at day 40 (Fig. 11b). This minimum is maintained until ~ day 80, when the current reintensifies to values of 80 cm s^{-1} or greater, which are maintained for the duration of the experiment. As in Case 1, the reintensification is consistent with a nonlinear feedback mechanism that becomes important at this time, i.e., strong thermal fronts, caused by the initial poleward advection, generate thermal winds that feed back to enhance the poleward flow at the surface.

The v and $\mathbf{c}$ fields for 350 m depth, corresponding to the average core depth of the undercurrent (see Fig. 18b) are presented in Figs. 12a,b. The initialization of the NW Shelf waters is seen at the inshore equatorward corner in Fig. 2f. The addition of the NW Shelf waters is sufficient to establish a stronger equatorward flow (10–50 cm s^{-1}) than was observed in Case 1.

(ii) *Generation of the eddies*

The addition of the NW Shelf waters creates a far more energetic and unstable current than in Case 1 and leads to a much earlier generation of eddies. The NW Shelf waters locally increase the barotropic instability near the source region, so that by day 10 (Fig. 11a) an eddy forms on the boundary of the NW Shelf waters.

The NW Shelf waters also increase the vertical shear by strengthening the surface poleward flow (Fig. 11b) and the equatorward undercurrent (Fig. 12a). As shown in the analysis section below, this vertical shear adds to the baroclinicity of the currents so that eddies are subsequently generated downstream from the

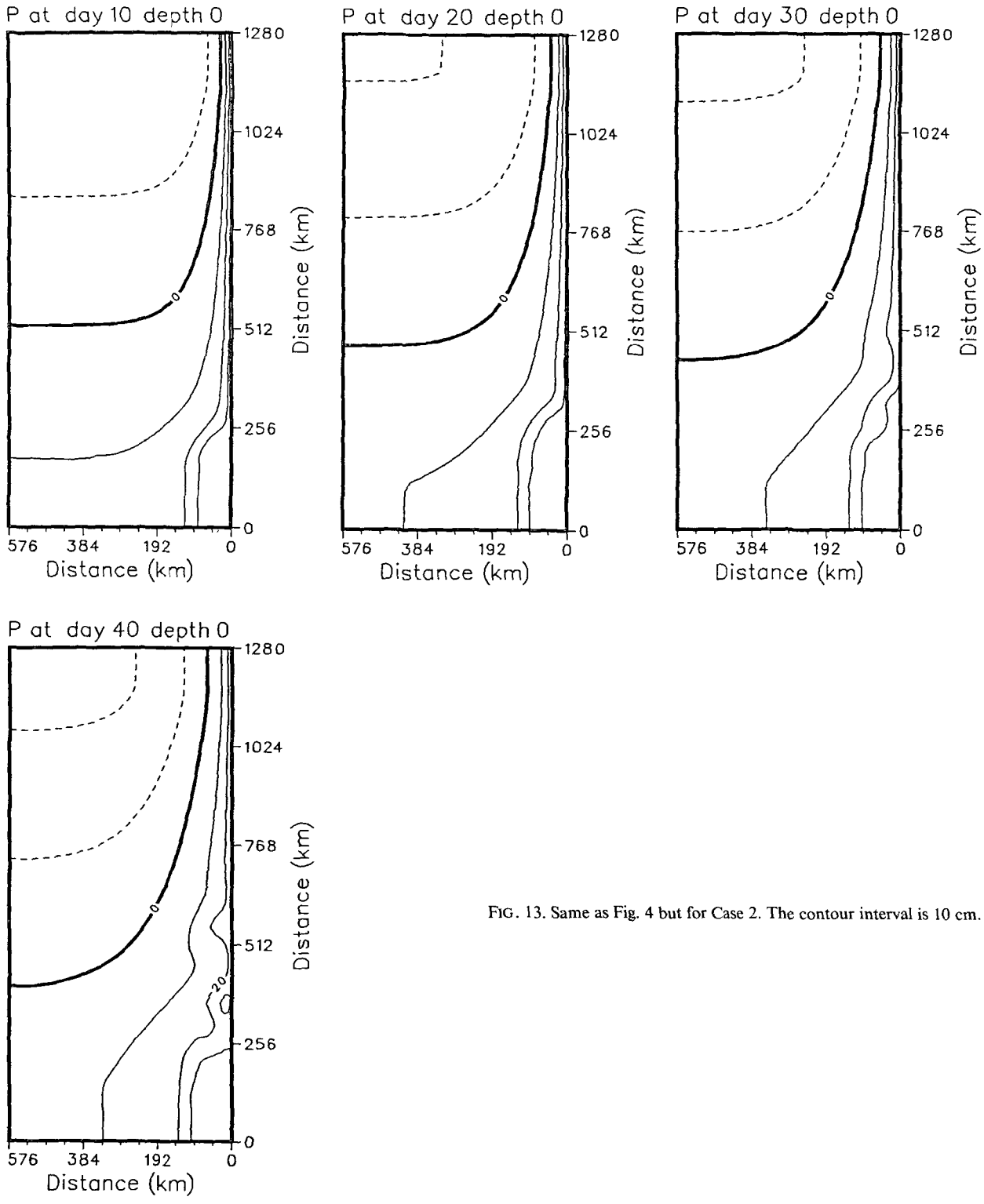

FIG. 13. Same as Fig. 4 but for Case 2. The contour interval is 10 cm.

source region through both baroclinic and barotropic instability processes.

The generation of the eddies is illustrated by the time evolution of the dynamic height fields (Fig. 13), which shows the generation of eddies first in the equatorward source region, and then, as time progresses, downstream from the source region. By day 80 eddies extend throughout the entire coastal domain and show growth

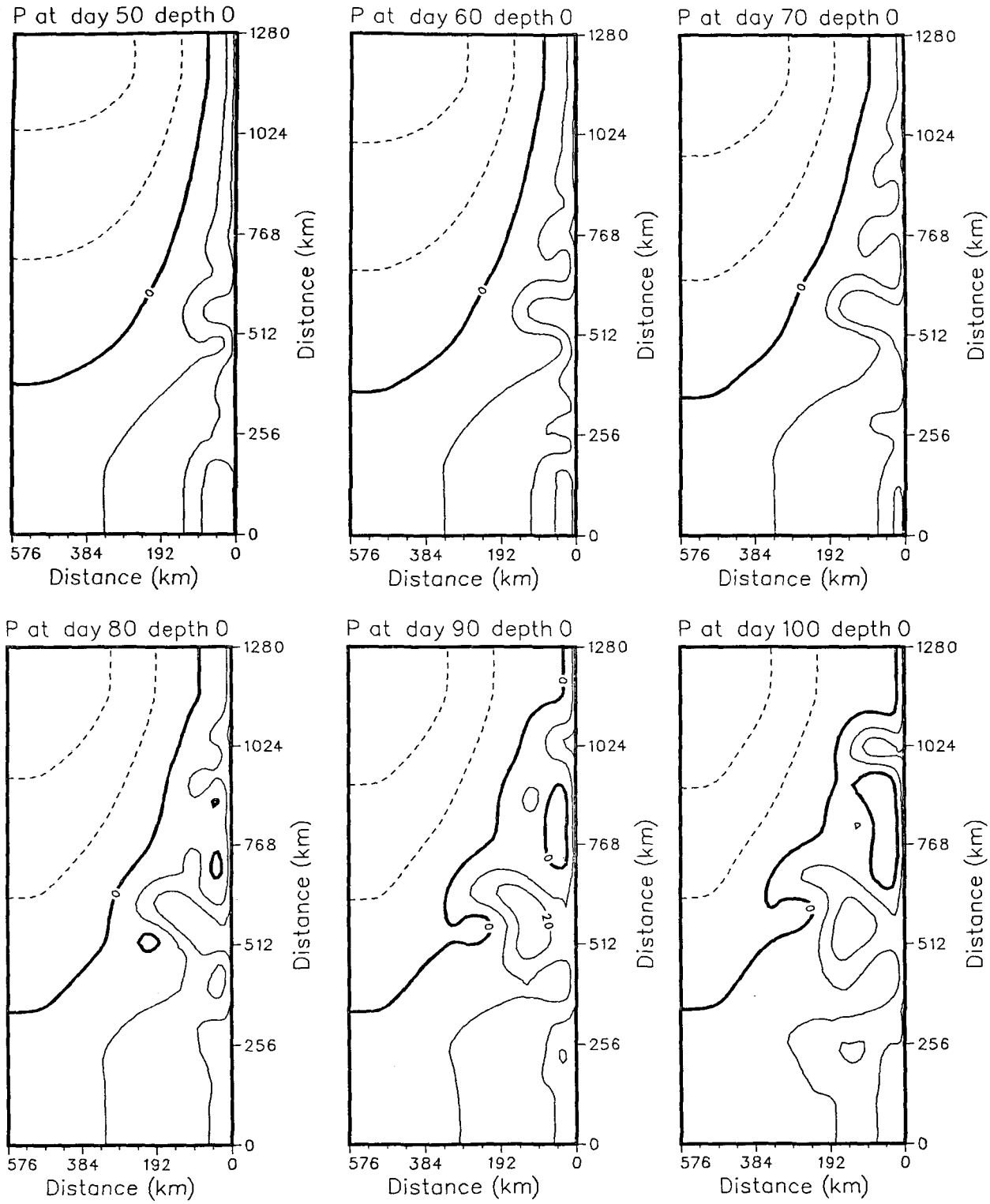

FIG. 13. (*Continued*)

and movement offshore. Generation of the eddies at the poleward end of the domain occurs at around the same time (days 70–90) as in Case 1, as expected, since the same alongshore temperature gradient, which was shown to be unstable toward the poleward end of the model domain, is retained in Case 2. The closed con-

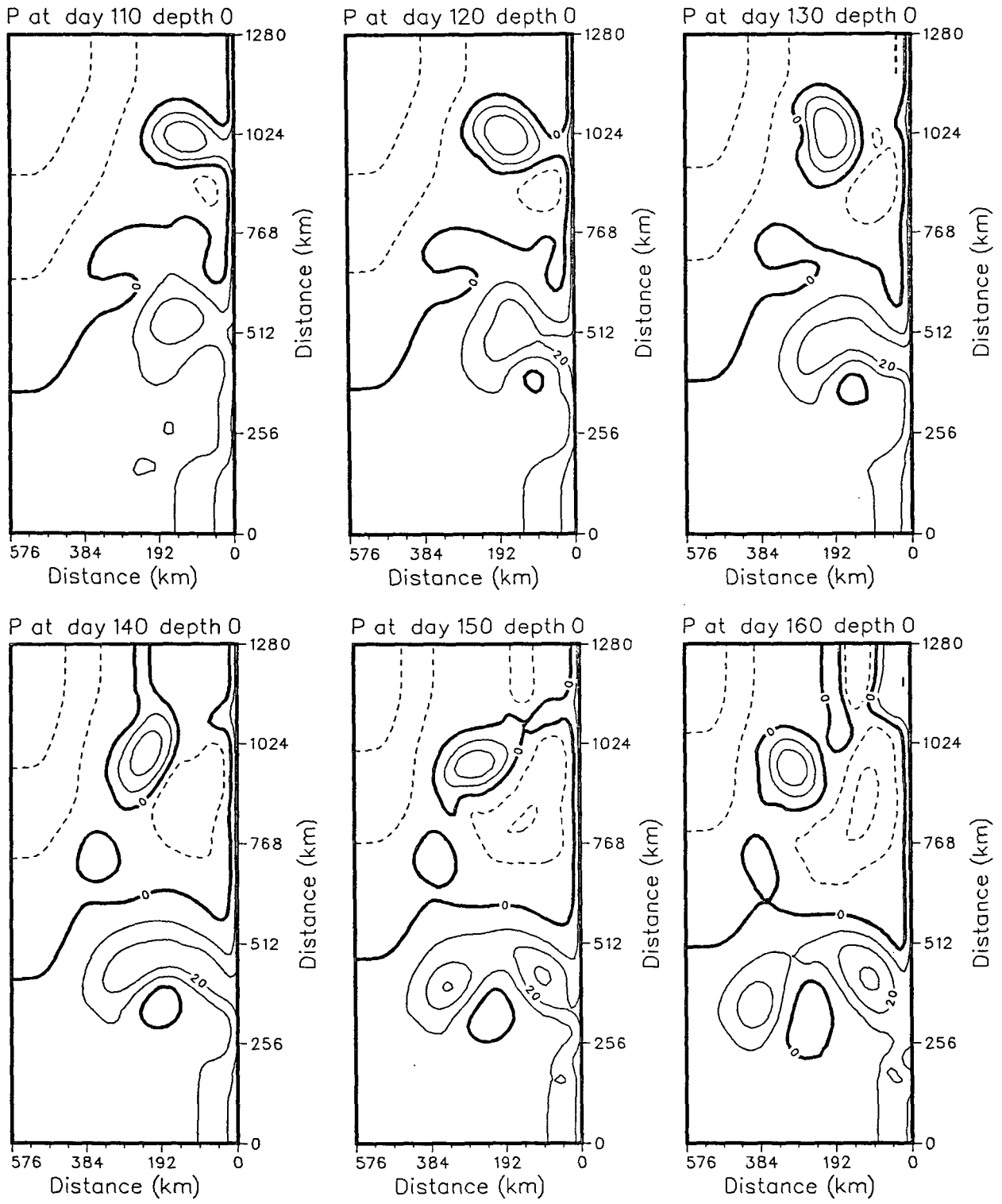

FIG. 13. (*Continued*)

tours on the temperature plot seen in Fig. 11c from day 80 on are associated with both cyclonic and anticyclonic rings (Figs. 11c and 13) forming alongshore. As seen in both the surface velocity and the dynamic height fields, at subsequent times these rings pinch off the offshore meanders, trap warm NW Shelf origin waters, and then move offshore. The rings also show a strong temperature structure (Fig. 11c) as the NW Shelf

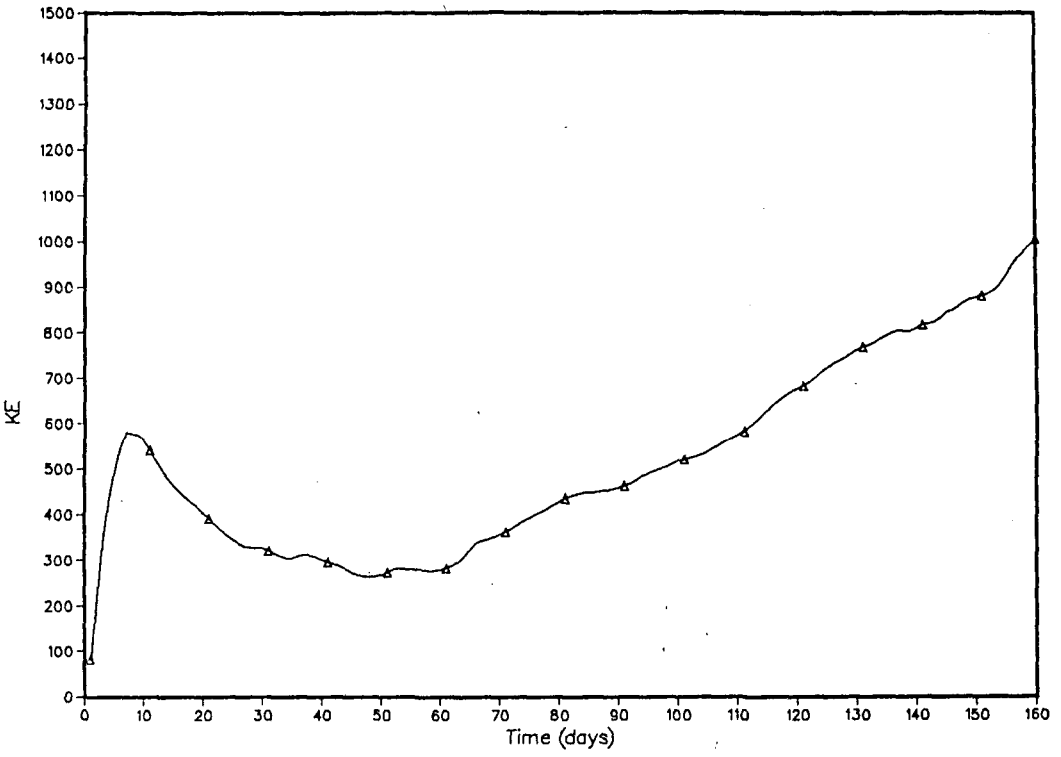

FIG. 14. Same as Fig. 6 but for Case 2.

waters, advected poleward, are cut off in the rings. The continued growth and offshore movement is seen at day 160.

As in Case 1, the magnitudes of the model alongshore currents in the poleward end of the domain compare favorably with the LUCIE current meter data obtained in the same vicinity, e.g., at Cape Mentelle. Unlike the results of Case 1, the magnitudes of the alongshore currents are significantly stronger at the equatorward end of the domain and along the entire coastal region. While a comparison of the model alongshore velocities at the poleward and interior parts of the model domain with the LUCIE mean current meter data in the same regions is favorable, the model alongshore velocities at the equatorward end of the domain may be too strong. For example, the LUCIE data at 65 m depth at Carnarvon (25°S) show a mean poleward velocity of 5.7 cm s^{-1} compared to the mean poleward model velocity of 13 cm s^{-1}. Some other factors not considered here, such as wind forcing, which would generally act in the opposite direction to the Leeuwin Current, could lead to lower current velocities, which would be more consistent with the current meter observations. The additional factor of wind forcing will be considered in a subsequent study by Batteen and Rutherford (1990).

2) ANALYSES OF EDDY GENERATION MECHANISMS

(i) *Energy analysis*

Because time series of total kinetic (Fig. 14) and available potential energy (not shown) showed that the kinetic energy became quasi-steady during days 30 to 60 before steadily growing again, days 30 to 40 were chosen for more detailed analysis. Over the same period, available potential energy (not shown) was quasi-steady and then decreased.

The energy transfer plots in Fig. 15 show strong transfers between the mean and eddy available potential energy (Fig. 15a) and strong barotropic transfer (Fig. 15c), all at the equatorward end of the domain. A comparison between the u velocity component fields on days 30 (not shown) and 40 (Fig. 15d) shows that eddy generation has occurred further poleward than shown in the transfers in Fig. 15. The transfers shown in Fig. 15 are much stronger than those leading to eddy development farther downstream so that the downstream transfers fail to show at the contour interval used.

Energy transfer diagrams (not shown) calculated over the upper five layers, and extending between 520 and 700 km alongshore (corresponding to the region of eddy generation shown at day 40 in Fig. 11a) showed that for the inshore 45 km, there was baroclinic instability and a negative barotropic transfer, while over the region extending from 45 km to 90 km offshore, the baroclinic contribution was weaker and barotropic instability was apparent.

(ii) *Spectral analysis*

The spectral energy plots at days 30 and 50 are shown in Figs. 16a and 16b. The strong growth from days 30

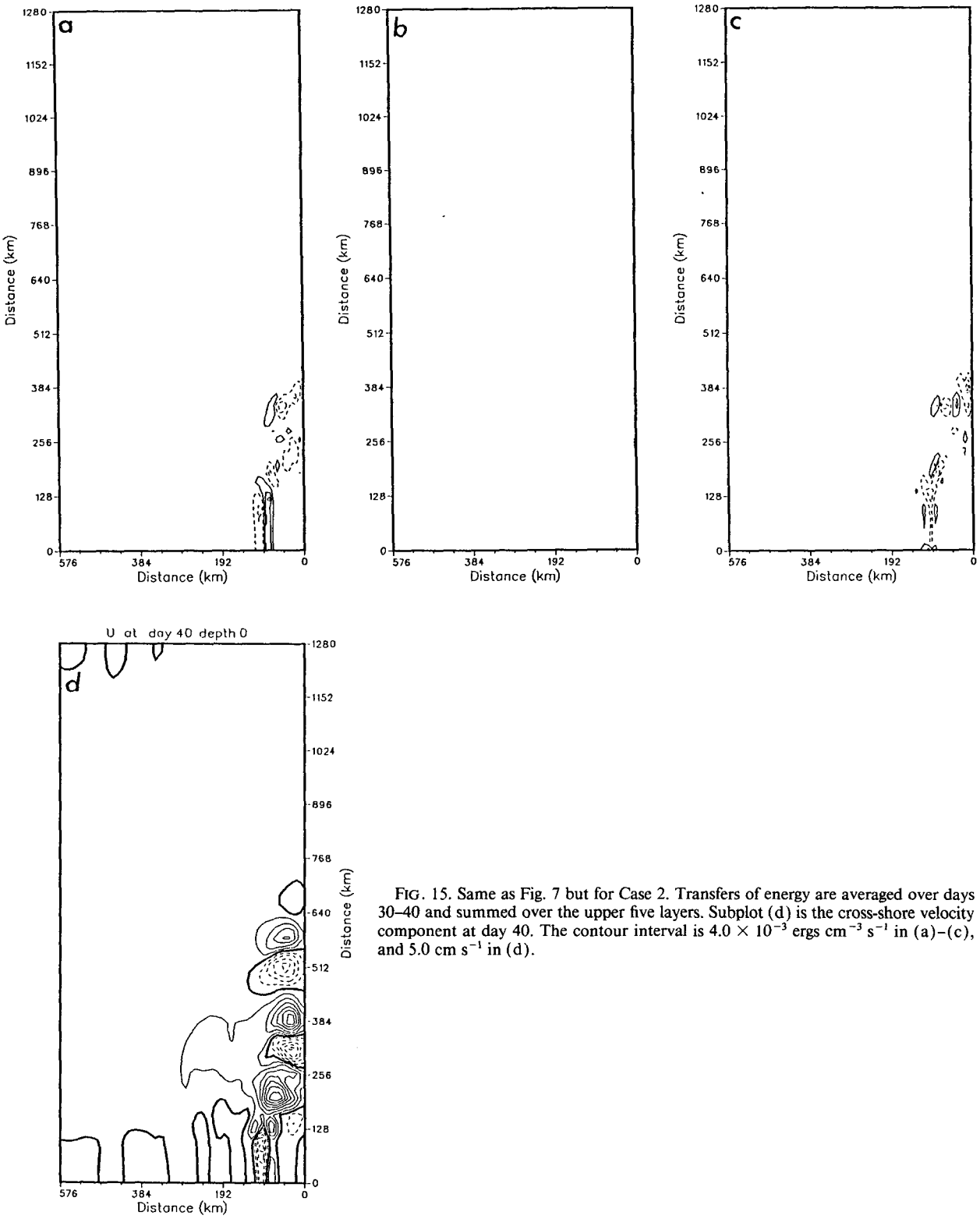

FIG. 15. Same as Fig. 7 but for Case 2. Transfers of energy are averaged over days 30–40 and summed over the upper five layers. Subplot (d) is the cross-shore velocity component at day 40. The contour interval is 4.0×10^{-3} ergs cm^{-3} s^{-1} in (a)–(c), and 5.0 cm s^{-1} in (d).

to 50 is seen in the peak developing at a 180 km wavelength (alongshore wavenumber of $\sim$0.0055 km^{-1}). At day 50 smaller peaks are also apparent at 100 km (alongshore wavenumber of $\sim$0.01 km^{-1}) and 65 km (alongshore wavenumber of $\sim$0.015 km^{-1}) scales. Whereas Case 1 had a single peak and barotropic growth was dominant, Case 2 has multiple spectral peaks during the eddy generation stage and strong

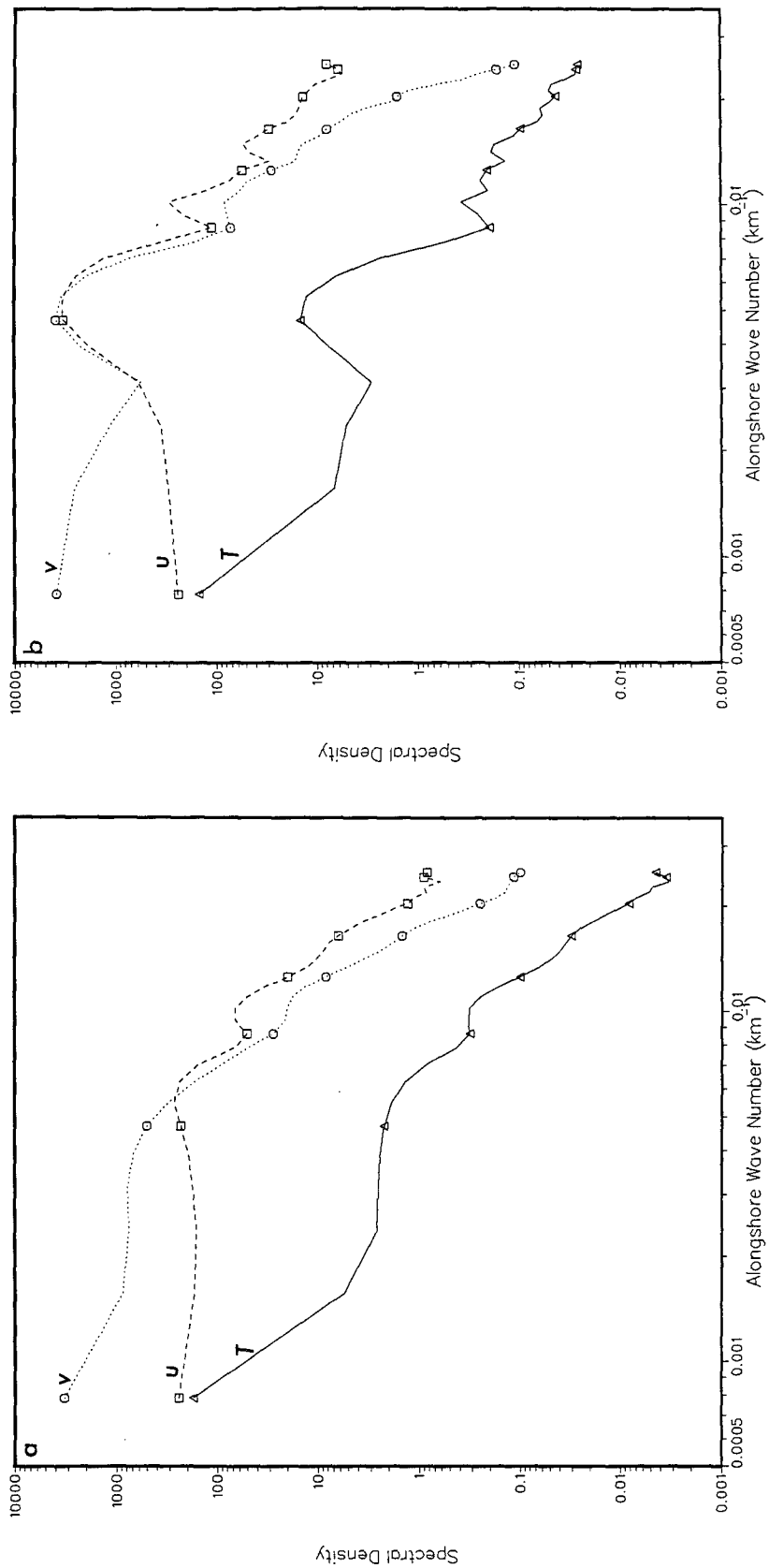

FIG. 16. Same as Fig. 8 but for Case 2 at days 30 (a) and 50 (b).

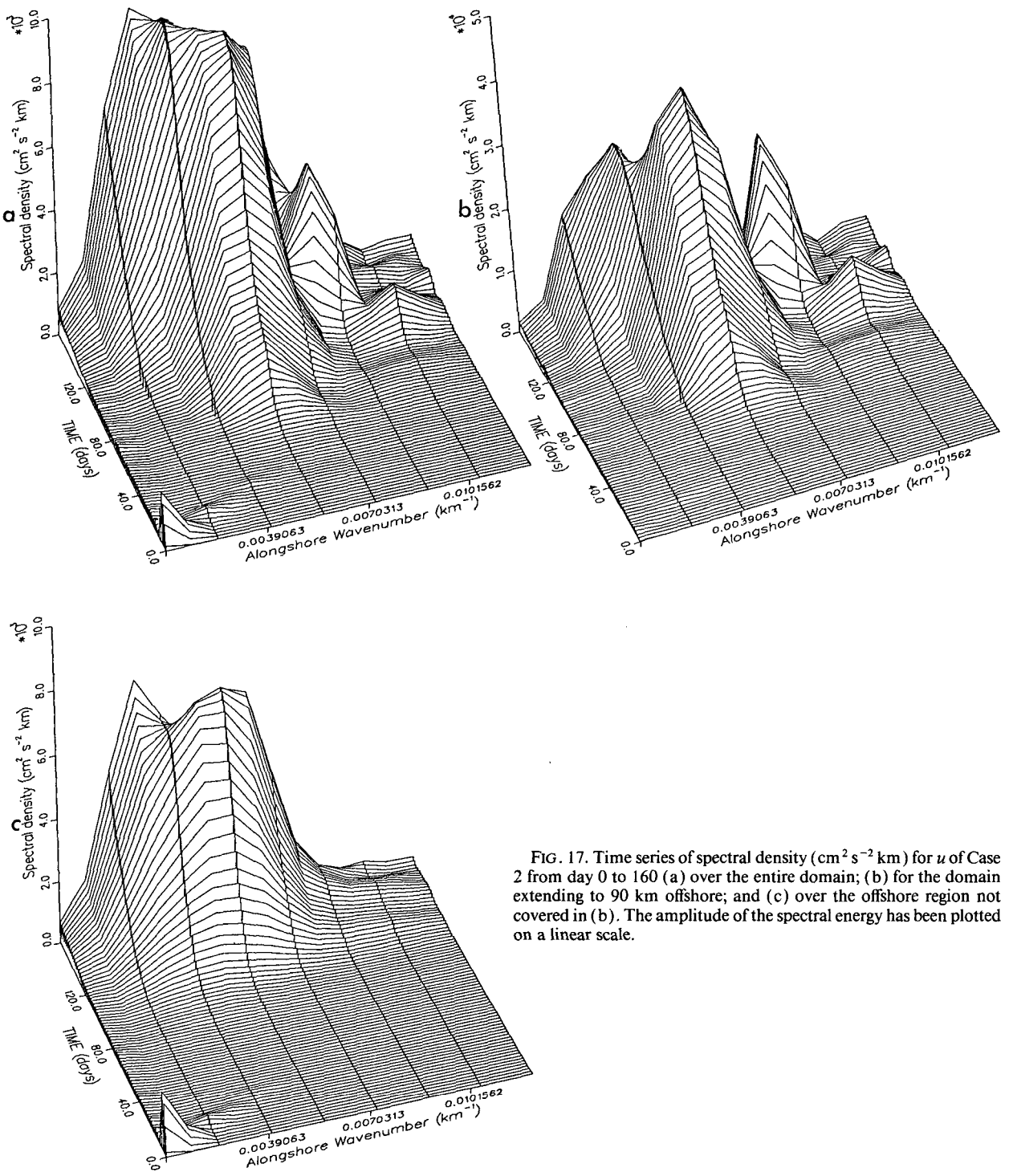

FIG. 17. Time series of spectral density ($cm^2 s^{-2}$ km) for u of Case 2 from day 0 to 160 (a) over the entire domain; (b) for the domain extending to 90 km offshore; and (c) over the offshore region not covered in (b). The amplitude of the spectral energy has been plotted on a linear scale.

baroclinicity is also a feature. It appears that when baroclinicity is strong, growth at multiple wavelengths occurs, possibly coinciding with other internal modes.

The spectral density for the entire 160 days of Case 2 is shown in Fig. 17a. The dominant scale of 180 km appears to broaden with time and a shift to larger scales is seen. To isolate the scales of generation and growth, a second spectral analysis was done over the inshore 90 km of the model, coinciding with the generation region. The spectral time series for the inshore region,

FIG. 18. Same as Fig. 10 but for Case 2. Time averaging is now over days 30–40, and the vertical cross sections are at 600 km alongshore, extending to 90 km offshore. Contour intervals are (a) 0.1°C m^{-1} s^{-1} and (b) 5.0 cm s^{-1}.

corresponding to the current, is shown in Fig. 17b and for the remainder of the domain in Fig. 17c. Inshore, the wavelength of the dominant growth in the vicinity of the current is near 180 km (alongshore wavenumber of ~0.0055 km^{-1}) and a secondary maximum occurs at 125 km (alongshore wavenumber of ~0.008 km^{-1}). Away from the core, Fig. 17c shows that the 180 km wavelength is dominant and that a shift to longer wavelengths occurs with time.

Comparing the results of the spectral analysis from Cases 1 and 2, the effects of the addition of NW Shelf waters may be determined. In the mainly barotropic Case 1, eddy generation and subsequent growth was at a wavelength of approximately 150 km. With the inclusion of the NW Shelf waters, and its strong baroclinic contribution toward instability, the main growth occurs at 180 km. The NW Shelf waters appear to increase the scale at which the dominant eddy growth occurs by modifying the thermal structure in the inshore region.

(iii) *Instability analysis*

Figure 18 is used to confirm that the necessary and sufficient conditions for the observed eddy generation are satisfied. In particular, the cross-shore derivative of potential vorticity (Fig. 18a) changes sign inshore, and its product with the mean alongshore flow (Fig. 18b) is clearly positive at some location in the domain, which satisfies the necessary conditions for baroclinic instability. The necessary conditions for an energy source for the eddy generation are satisfied by both the vertical and horizontal shears in the flow.

The Rossby radius of deformation was calculated for the region of instability as 27.9 km. Comparing this value with that of Case 1 (27.6 km), little change has occurred to the radius of deformation despite the inclusion of the NW Shelf waters.

(iv) *Conclusions*

The current, driven by a combination of Indian Ocean and NW Shelf thermal forcing, is much more vigorous and unstable than Case 1, forced by the Indian Ocean alone. Barotropic instability is strong at the equatorward end, near the source of the NW Shelf waters. The addition of the NW Shelf waters adds strongly to the baroclinicity of the current inshore, although the Rossby radius remains virtually unchanged. The barotropic contribution at the offshore edge of the core of the current is also slightly increased by the presence of the NW Shelf waters. The dominant scale of eddy generation in the current is 180 km. This is consistent with the calculated Rossby radius of ~28 km in the strongly baroclinic flow. This wavelength is, like Case 1, consistent with the Rossby deformation length scale of eddies found in the strong poleward flow over the slope by Golding and Symonds (1978) and Andrews (1983). Away from the current, a spectral shift towards longer wavelengths is seen, consistent with the growth of eddies as they move offshore.

4. Conclusions

A full primitive equation (PE) model was initialized with climatological data to investigate the generation and stability of the Leeuwin Current and its associated eddies. Initializations were done using climatological mean temperatures for the Indian Ocean and NW Shelf. The ocean was then allowed to geostrophically adjust in the absence of external forcing. The currents generated by the model were unstable in both experi-

ments and mesoscale features were observed. To examine the dynamical reasons for the generation and stability of the eddies, a series of analysis techniques were applied to each experiment and the instability mechanisms and dominant length scales determined. A comparison with available observations was also made. A summary of the results from each of the two phases of this study, generation and instability, is presented below.

a. Leeuwin Current generation

The results of Case 1 showed that the Indian Ocean temperature structure is sufficient to drive an unstable poleward surface flow (the Leeuwin Current) and an equatorward undercurrent. The undercurrent rises as it flows equatorward and weakens in intensity. The surface current is augmented by onshore geostrophic inflow and accelerates downstream.

The results of Case 2 showed that the inclusion of the NW Shelf waters completely dominates in the NW Shelf equatorial source region. The effects of the NW Shelf waters weaken away from the source region but they continue to augment the Indian Ocean forcing, resulting in a stronger flow along the entire coastal boundary.

The results of both cases showed that, consistent with Weaver and Middleton (1989), after the surface current reaches its largest velocity, it subsequently broadens and drifts westward through baroclinic Rossby wave propagation. After about 80 days the surface current at the poleward end of the domain intensifies again, which, consistent with Weaver and Middleton (1989), is due to a feedback mechanism that becomes important at this time. In particular, the strong offshore fronts, caused by the initial poleward advection, generate thermal winds that feed back to enhance the poleward flow at the surface. These strong current magnitudes are maintained throughout the duration of the experiments (i.e., days 80–160).

The currents generated by the model agree well with the Leeuwin Current Interdisciplinary Experiment (LUCIE) current meter observations obtained during the austral fall and winter when the Leeuwin Current is observed, and other recent modeling studies.

b. Instability and eddies

The current driven by the Indian Ocean temperature gradient (Case 1) is unstable at the poleward end of the domain. In this region, instability is mixed, with barotropic instability dominant. Eddy generation occurs on the offshore side of the core of the current, consistent with the buoy observations of Cresswell and Golding (1979, 1980). The eddies have time scales of months, and wavelengths of $\sim$150 km, a scale consistent with the Rossby radius of deformation of 27.6 km and the mixed instability mechanism. The dominant type of rotation for the eddies is anticyclonic. The anticyclonic, westward propagating eddy at the poleward end of the model domain ($y \sim 1024$ km) is reminiscent of observations by Cresswell and Golding (1979) and Godfrey et al. (1979) of a semipermanent anticyclonic eddy located west of Cape Naturaliste (33.5°S).

The addition of the NW Shelf waters (Case 2) creates a far more energetic and unstable current. The NW Shelf waters increase the vertical shear by strengthening the surface flow and the undercurrent and hence add to the baroclinicity of the current. The NW Shelf waters also locally increase the barotropic instability near the source region. The dominant wavelength associated with eddies developing in the current forced by the Indian Ocean and NW Shelf water density fields is 180 km. The NW Shelf waters appear to increase the scale at which the dominant eddy growth occurs by modifying the thermal structure in the inshore region. The eddies have time scales of months, consistent with buoy observations (e.g., Cresswell and Golding 1979). Both cyclonic and anticyclonic eddies are observed, consistent with observations (e.g., Hamon 1965, 1972).

In both cases, the dominant length scales of eddies are close to the wavelength associated with a low-mode Rossby radius of deformation, consistent with observations (e.g., Golding and Symonds 1978; Andrews 1983; Griffiths and Pearce 1985) and laboratory studies (Condie and Ivey 1988) of the Leeuwin Current.

This study has shown that the Leeuwin Current can be successfully modeled using a PE model forced by the mean climatology. Consistent with the findings of Weaver and Middleton (1989), a shelf is not required to produce and maintain the current. The mesoscale features that have been missing from previous modeling studies are produced by the model and at scales comparable with available observations.

Acknowledgments. This work was supported by the National Science Foundation under Grant OCE 8809465 and by direct funding at the Naval Postgraduate School (NPS) with the Office of Naval Research as the sponsor. Computer resources were provided by the W.R. Church Computer Center at NPS. The authors wish to thank Tim Stanton for his assistance with the spectral analysis techniques used in the study, and Craig S. Nelson, Andrew J. Weaver, and J. Stuart Godfrey for comments on an earlier version of the manuscript. MLB also wishes to thank Jorg Imberger for his generous hospitality at the Centre for Water Research at the University of Western Australia, where MLB conducted preliminary research on the Leeuwin Current in the austral summer of 1988.

APPENDIX

Analysis Techniques

A description of the energy, spectral and stability techniques used to analyze the generation and stability of the Leeuwin Current and eddies is presented here.

1. Energy analysis

An energy analysis based on that of Han (1975) and Semtner and Mintz (1977) is made to gain a better understanding of the energy transfers in the unstable flow. The energy calculations are presented using the Semtner and Mintz (1977) notation:

$(\bar{})$	time average
$(\,)'$	time deviation
$(\tilde{})$	horizontal space average
$(\,)^*$	horizontal space deviation.

The kinetic energy (K) is calculated by

$$K = \frac{u^2 + v^2}{2} \tag{1}$$

and presented in a time series plot. After reaching a quasi-steady state in which the total kinetic energy is nearly constant, the time mean and time eddy kinetic energy are calculated by

$$\bar{K} = \frac{\overline{u}^2 + \overline{v}^2}{2} \tag{2}$$

$$K' = \frac{\overline{u'^2} + \overline{v'^2}}{2}. \tag{3}$$

Available potential energy (P) is calculated by

$$P = \alpha g\left[\frac{1}{2}(T^*)^2\left(\frac{\partial \tilde{T}}{\partial z}\right)^{-1}\right] \tag{4}$$

and plotted in a time series to determine when a quasi-steady state is reached and statistics can be collected. The temporal mean and eddy available potential energy are then calculated by

$$\bar{P} = \alpha g\left[\frac{1}{2}(\overline{T^*})^2\left(\frac{\partial \tilde{\bar{T}}}{\partial z}\right)^{-1}\right] \tag{5}$$

$$P' = \alpha g\left[\frac{1}{2}(\overline{T'^*})^2\left(\frac{\partial \tilde{\bar{T}}}{\partial z}\right)^{-1}\right]. \tag{6}$$

The transfers between the energy types are defined, after Semtner and Mintz (1977), by

$$\{\bar{K} \rightarrow \bar{P}\} = -\alpha g[\bar{T}\bar{w}] \tag{7}$$

$$\{P' \rightarrow K'\} = \alpha g[\overline{T'w'}] \tag{8}$$

$$\{\bar{K} \rightarrow K'\} = \bar{\mathbf{v}} \cdot \left(\nabla \cdot \overline{\mathbf{v}'\mathbf{v}'} + \frac{\partial}{\partial z}\overline{w'\mathbf{v}'}\right) \tag{9}$$

$$\{\bar{P} \rightarrow P'\} = \alpha g\left[\overline{T^*\nabla \cdot \mathbf{v}'T'^*}\left(\frac{\partial \tilde{\bar{T}}}{\partial z}\right)^{-1}\right]. \tag{10}$$

The model output consists of velocity components and temperature at daily intervals at each gridpoint; neither the vertical velocity nor any advection terms calculated by the model are stored. As the calculation of the energy transfers requires both vertical velocity and numerous advection terms, these were recalculated in the same manner as in the model but using the stored values of u, v and T as the input data. Although the energy transfers are recalculated from model output, they are consistent with the initial calculations of vertical velocity and advection terms in the model.

Using the energy transfers calculated above and the temporal mean and eddy kinetic and available potential energy values, an energy transfer diagram may be constructed for those periods in which the total energies are nearly constant. Semtner and Mintz (1977) applied their energy transfer analysis to currents that had become unstable, generated eddies and then reached a quasi-steady state. In this study, the steady energetic state prior to eddy generation is examined and the energy transfer plots and diagrams used to argue for the instability mechanism that leads to the initial eddy generation in each case.

2. Spectral analysis

A spectral analysis technique is used to estimate the dominant wavelengths at which eddy growth occurs. The time evolution of the eddy fields can be seen on three-dimensional time series plots of spectral density versus alongshore wavenumber. The alongshore wavenumber is selected based on an assumption of a meridional anisotropic preference for the eddy development. The model configuration of 65 alongshore temperature gridpoints and 64 velocity points is ideal in allowing data over the entire domain to be used to compute the discrete Fourier transform based on 64 points. Leakage due to the finite length of the series is reduced using a Hanning window. The loss of variance due to the windowing is then compensated by scaling the calculated one-sided spectral density appropriately.

3. Stability analysis

The stability analysis used in this study is based on Batteen et al. (1989), who investigated the dynamics of the eddy generation observed in the PE model. The potential for instability is determined by examining the potential vorticity (q) of the flow and also its cross-shore derivative ($\partial q/\partial x$). The potential vorticity is calculated by

$$q \sim (f + \zeta)\frac{\partial T}{\partial z} - \frac{\partial T}{\partial x}\frac{\partial v}{\partial z} \tag{11}$$

where

$$\zeta = \frac{\partial v}{\partial x} - \frac{\partial u}{\partial y}. \tag{12}$$

For a flow that has a basic state changing slowly in space and time, Kamenkovich et al. (1986) give the necessary conditions for baroclinic instability as: $\partial q/\partial x$ changes sign, and $\bar{v}\partial q/\partial x$ must be positive somewhere in the flow. They also give sufficient conditions

for the instability mechanisms. For baroclinic instability, the source of energy is the vertical shear in the mean flow ($\partial\bar{v}/\partial z$) and the scale of the generated disturbances is of the order of the Rossby radius of deformation. For barotropic instability, the energy source is the horizontal shear in the mean flow ($\partial\bar{v}/\partial x$) and the disturbances grow at a scale less than the Rossby radius.

The sufficient condition for baroclinic instability (Kamenkovich et al. 1986) of a minimum vertical shear is not required for this study as the mean flow is strongly meridional. Olivier (1987) showed that on a β-plane, energy can be released in a meridional flow without being acted upon by β; hence any vertical shear which is greater than the dissipation level in the model may produce instability.

The individual components of the analysis, namely energy transfers, spectral analysis and the instability analysis, should all complement each other. From the energy transfer analysis, the location and magnitude of baroclinic and barotropic transfers can be found. Those waves that are unstable and, in particular, the fastest growing wave can be determined from the internal Rossby radii, and the spectra can confirm whether those waves could exist.

REFERENCES

Allen, J. S., 1980: Models of wind-driven currents on the continental shelf. *Annual Reviews of Fluid Mechanics,* Vol. 12, Annual Reviews, 389–433.

Andrews, J. C., 1977: Eddy structure and the West Australian Current. *Deep-Sea Res.,* **24,** 1133–1148.

——, 1983: Ring structure in the poleward boundary current off Western Australia in summer. *Aust. J. Mar. Freshwater Res.,* **34,** 547–561.

Arakawa, A., and V. R. Lamb, 1977: Computational design of the basic dynamical processes of the UCLA general circulation model. *Methods Comput. Phys.,* **17,** J. Chang, Ed., Academic Press, 173–265.

Batteen, M. L., and Y.-J. Han, 1981: On the computational noise of finite-difference schemes used in ocean models. *Tellus,* **33,** 387–396.

——, and M. J. Rutherford, 1990: A numerical study of wind and thermal forcing effects on the ocean circulation off Western Australia. *J. Phys. Oceanogr.,* submitted.

——, R. L. Haney, T. A. Tielking and P. G. Renaud, 1989: A numerical study of wind forcing of eddies and jets in the California Current System. *J. Mar. Res.,* **47,** 493–523.

Boland, F. M., J. A. Church, A. M. G. Forbes, J. S. Godfrey, A. Huyer, R. L. Smith and N. J. White, 1988: Current-meter data from the Leeuwin Current Interdisciplinary Experiment. CSIRO Australia Marine Laboratories Rep. No. 198, 31 pp.

Camerlengo, A. L., and J. J. O'Brien, 1980: Open boundary conditions in rotating fluids. *J. Comput. Phys.,* **35,** 12–35.

Church, J. A., G. R. Cresswell and J. S. Godfrey, 1989: The Leeuwin Current. *Poleward Flows along Eastern Ocean Boundaries,* S. Neshyba, Ch. N. K. Mooers, R. L. Smith and R. T. Barber, Eds., Springer-Verlag Lecture Notes, 230–252.

Colborn, J. G., 1975: The thermal structure of the Indian Ocean. International Indian Ocean Expedition Monogr. No. 2.

Condie, S. A., and G. N. Ivey, 1988: Convectively driven coastal currents in a rotating basin. *J. Mar. Res.,* **46,** 473–494.

Cresswell, G. R., and T. J. Golding, 1979: Satellite-tracked buoy data report III. Indian Ocean 1977, Tasman Sea July–December 1977. CSIRO Australia Division of Fisheries and Oceanography Rep. 101.

——, and ——, 1980: Observations of a south-flowing current in the southeastern Indian Ocean. *Deep-Sea Res.,* **27A,** 449–466.

Dakin, W. J., 1919: The Percy Sladen Trust Expeditions to the Abrolhos Islands (Indian Ocean). Rep. 1. *J. Linnean Soc.,* **34,** 127–180.

Gentilli, J., 1972: Thermal anomalies in the Eastern Indian Ocean. *Nature (London) Phys. Sci.,* **238,** 93–95.

Godfrey, J. S., and K. R. Ridgway, 1985: The large-scale environment of the poleward-flowing Leeuwin Current, Western Australia: Longshore steric height gradients, wind stresses and geostrophic flow. *J. Phys. Oceanogr.,* **15,** 481–495.

——, and A. J. Weaver, 1990: Is the Leeuwin Current driven by Pacific heating and winds? *Progress in Oceanography,* Pergamon, submitted.

——, D. J. Vaudrey and S. D. Hahn, 1986: Observations of the shelf-edge current south of Australia, winter 1982. *J. Phys. Oceanogr.,* **16,** 668–679.

Golding, T. J., and G. Symonds, 1978: Some surface circulation features off Western Australia during 1973–1976. *Aust. J. Mar. Freshwater Res.,* **29,** 187–191.

Griffiths, R. W., and A. F. Pearce, 1985: Instability and eddy pairs on the Leeuwin Current south of Western Australia. *Deep-Sea Res.,* **32,** 1511–1534.

Hamon, B. V., 1965: Geostrophic currents in the south-eastern Indian Ocean. *Aust. J. Mar. Freshwater Res.,* **16,** 255–271.

——, 1972: Geopotential topographies and currents off Western Australia, 1965–69. CSIRO Australia Division of Fisheries and Oceanography Tech. Paper No. 32.

——, and G. R. Cresswell, 1972: Structure functions and intensities of ocean circulation off east and west Australia. *Aust. J. Mar. Freshwater Res.,* **23,** 99–103.

Han, Y.-J., 1975: Numerical simulation of mesoscale eddies. Ph.D. thesis, University of California, Los Angeles, 154 pp.

Holland, W. R. 1978: The role of mesoscale eddies in the general circulation of the ocean-numerical experiments using a wind-driven quasi-geostrophic model. *J. Phys. Oceanogr.,* **8,** 363–392.

——, and M. L. Batteen, 1986: The parameterization of subgrid scale heat diffusion in eddy-resolved ocean circulation models. *J. Phys. Oceanogr.,* **16,** 200–206.

Holloway, P. E., and H. C. Nye, 1985: Leeuwin Current and wind distributions on the southern part of the Australian North West Shelf between January 1982 and July 1983. *Aust. J. Mar. Freshwater Res.,* **36,** 123–137.

Hsiung, J., 1985: Estimates of the global oceanic meridional heat transport. *J. Phys. Oceanogr.,* **15,** 1405–1413.

Huyer, A., 1990: Shelf circulation. *The Sea: Ocean Engineering Science* B. Le Mehaute, D. M. Hanes, Eds. **9,** 423–466.

Kamenkovich, V. M., M. N. Koshlyakov and A. S. Monin, 1986: *Synoptic Eddies in the Ocean.* D. Riedel, 433 pp.

Kitani, K., 1977: The movement and physical characteristics of the water off Western Australia in November 1975. *Bull. Far Seas Fish. Res. Lab. (Shimizu),* **15,** 13–19.

Kundu, P. J., and J. P. McCreary, 1986: On the dynamics of the throughflow from the Pacific into the Indian Ocean. *J. Phys. Oceanogr.,* **16,** 2191–2198.

Levitus, S., 1982: Climatological Atlas of the World Ocean. NOAA Prof. Paper 13. US Department of Commerce: Washington, DC.

Markina, N. P., 1976: Biogeographic regionalization of Australian waters of the Indian Ocean. *Oceanology,* **15,** 602–604.

McCreary, J. P., S. R. Shetye and P. K. Kundu, 1986: Thermohaline forcing of eastern boundary currents: With application to the circulation off the west coast of Australia. *J. Mar. Res.,* **44,** 71–92.

Olivier, D. A., 1987: Numerical simulations of the California Current: Filament formation as related to baroclinic instability. M.S. thesis, Naval Postgraduate School, 69 pp.

Parrish, R. H., A. Bakun, D. M. Husby and C. S. Nelson, 1983:

Comparative climatology of selected environmental processes in relation to eastern boundary current pelagic fish reproduction. Sharp, G. D., J. Csirke, Eds., *Proc. Expert Consultation to Examine Changes in Abundance and Species of Neritic Fish Resources,* San Jose, Costa Rica, FAO Fish Rep. 291, Vol. 3, 731–778.

Pearce, A. F., and G. R. Cresswell, 1985: Ocean circulation off Western Australian and the Leeuwin Current. CSIRO Australia Division of Oceanography Information Service Sheet No. 16-3.

Rochford, D. J., 1962: Hydrology of the Indian Ocean. Part II: The surface waters of the south-east Indian Ocean and Arafura Sea in the spring and summer. *Aust. J. Mar. Freshwater Res.,* **13,** 226–251.

——, 1969: Seasonal variations in the Indian Ocean along 110°E. I. Hydrological structure of the upper 500 m. *Aust. J. Mar. Freshwater Res.,* **20,** 1–50.

——, 1986: Seasonal changes in the distribution of Leeuwin Current waters off southern Australia. *Aust. J. Mar. Freshwater Res.,* **37,** 1–10.

Saville-Kent, W., 1897: *The Naturaliste in Australia.* Chapman and Hall.

Semtner, A. J., and Y. Mintz, 1977: Numerical simulation of the Gulf Stream and mid-ocean eddies. *J. Phys. Oceanogr.,* **7,** 208–230.

Thompson, R. O. R. Y., 1984: Observations of the Leeuwin Current off Western Australia. *J. Phys. Oceanogr.,* **14,** 623–628.

——, 1987: Continental-shelf-scale model of the Leeuwin Current. *J. Mar. Res.,* **45,** 813–827.

——, and G. Veronis, 1983: Poleward boundary current off Western Australia. *Aust. J. Mar. Freshwater Res.,* **34,** 173–185.

Weatherly, G. L., 1972: A study of the bottom boundary layer of the Florida Current. *J. Phys. Oceanogr.,* **2,** 54–72.

Weaver, A. J., and J. H. Middleton, 1989: On the dynamics of the Leeuwin Current. *J. Phys. Oceanogr.,* **19,** 626–648.

——, and ——, 1990: An analytic model for the Leeuwin Current off Western Australia. *Contin. Shelf Res.,* 105–122.

Wyrtki, K., 1962: Geopotential topographies and associated circulation in the south-eastern Indian Ocean. *Aust. J. Mar. Freshwater Res.,* **13,** 1–17.